Neural Correlates of Countermanding Saccade Deficits in Parkinson's Disease

Min Wah Leung

Thesis submitted to the Neuroscience Graduate Program in partial fulfillment of the requirements for the Master of Science degree in Neuroscience

Department of Cellular and Molecular Medicine

Faculty of Medicine

University of Ottawa

Abstract

Parkinson's Disease is characterized by the loss of dopaminergic neurons in the substantia nigra pars compacta (SNc). The SNc supplies the basal ganglia (BG) via dopaminergic projections which innervate D1 and D2 receptors that mediate motor control. The BG also mediates cognitive processes and eye movement, parallel to its involvement in motor control. Behavioural correlates of PD have been established from previous countermanding tasks and population neural activity has been shown to correlate with PD disease state, but a reliable means to find patient-specific biomarkers of disease remains unknown. Here, we propose using eye movements and electroencephalography (EEG) to capture neural correlates of dysfunction in PD. We have developed a novel saccade-based stop-signal task in VR that probes the subject's ability to recruit the neural processes involved in action selection and response inhibition. We have tested this system on 7 healthy subjects and verified that we could identify key signature changes in the EEG profile during left and right saccade, countermand, and antisaccades similar to those found in similar reach tasks. The successful completion of a countermand (revoking a planned action) stop trial requires large synchronization of frontal theta and motor beta activity, representing the BG-thalamocortical loop recruiting the necessary processes to inhibit motor responses. The pattern in the event-related potentials that illustrates this is a strong event-related synchronization (ERS) peak followed by an event-related desynchronization (ERD) dip, and increased weights in the scalp topology at the frontal-parietal region. Since tasks involving response inhibition serve to probe the subject's ability to revoke a planned action, it does not matter whether the task was completed using hand movements or saccades. Our ERP isolated from Independent Component Analysis (ICA) resembles the ERP from previous literature, and exhibits increased weights on the sensorimotor region with a narrow band beta. This narrow band beta range is subject-specific and can be better visualized by using a modelling approach called FOOOF (fitting oscillations one over f). Lastly, the increased decoding performance in each subject's successive recording session suggests that using subject-specific features positively biases the model towards enhanced generalizability. Our experimental platform provides a robust framework that accounts for trial-by-trial variability, and can capture the presence of and evoke beta oscillations in healthy subjects.

Acknowledgements

I would like to thank my supervisors Dr. Adam J. Sachs, Dr. Leonard Maler, and my mentor Dr. Chadwick Boulay for providing me the opportunities and relevant knowledge to develop tools in neurosurgery research. The support from the Sachs lab helped drive my project forward, and I would like to extend my heartfelt thanks to each member. I would also like to thank the members of my thesis advisory committee, Dr. Richard Naud and Dr. Jean-Claude Beique, for their continued encouragement towards the completion of this thesis.

The Parkinson Research Consortium made this project possible, and I thank the Toth Family for their support in funding the research and prospective cure for Parkinson's Disease.

Abbreviations

Basal Ganglia	BG
Parkinson's Disease	PD
Substantia Nigra pars Compacta	SNc
Substantia Nigra pars Reticulata	SNr
Subthalamic Nucleus	STN
Globus Pallidus Interna	GPi
Globus Pallidus Externa	GPe
Mesencephalic Locomotor Region	MLR
Pedunculopontine nucleus	PPN
Electroencephalography	EEG
Deep Brain Stimulation	DBS
Source Power Comodulation	SPoC
Common Spatial Patterns	CSP
Filter Bank Common Spatial Patterns	FBCSP
Independent Component Analysis	ICA
Fast Fourier Transform	FFT
Finite Impulse Response	FIR
Infinite Impulse Response	IIR
Application Programming Interface	API

Contents

1 Chapter 1: Neuroengineering Correlates of Parkinson's Disease

Planning and executing controlled movements involves the precise coordination of multiple circuits of the brain. Initiating such movements and planning the next involve a complex interplay within and between different areas of the brain, such as the cerebellum in the timing and the basal ganglia (BG) in the generation of movement. The BG adjust the amount of force associated with each movement, and damage to the BG typically results in too much (involuntary) or too little (rigidity) activation of movement [1–3]. The BG comprise of multiple large subcortical structures located in the forebrain, diencephalon, and midbrain, as well as parallel circuits that modulate the associative, motor, and limbic systems [4].

The basal ganglia include the striatum (caudate, putamen, nucleus accumbens), the subthalamic nucleus (STN), the globus pallidus (internal and external segment), and the substantia nigra (pars compacta and pars reticulata) [5]. These subcortical structures can be categorized into three main groups: the input nuclei, output nuclei, and intrinsic nuclei [6]. The input nuclei are composed of the caudate, putamen, and nucleus accumbens, and receive information from the cortex, thalamus, and nigral sources. The output nuclei send BG information to the thalamus and are composed of the globus pallidus interna (GPi) and the substantia nigra pars reticulata (SNr). The intrinsic nuclei are involved in relaying information between the input and output nuclei, include the globus pallidus externa (GPe), STN, and the substantia nigra pars compacta (SNc). The striatum and STN receive the majority of inputs from the cerebral cortex and thalamic nuclei [5,7]. The output structures of the BG project GABAergically to the internal globus pallidus, ventral pallidum, and the SNr.

1.1 Dysfunctional Thalamo-Cortico BG Loop From Loss of DA in SNc

Parkinson's disease (PD) is characterized by loss of dopaminergic input from substantia nigra pars compacta (SNc) to the basal ganglia (BG). The motor dysfunction in PD is thought to be due to an imbalance between the direct and indirect pathways through the BG-thalamocortical network that is normally mediated by D1 and D2 receptors [8], respectively. Both pathways

facilitate smooth motor control, and the disruption of the indirect pathway caused by PD may result in rigidity and bradykinesia[9].

1.2 Neuroengineering Manifestation of Dysfunctional Network

The resting state dynamics of the BG-thalamocortical network are altered in the parkinsonian state, resulting in excessive synchronization of neural ensembles in the beta frequency range (13-30 Hz)[10,11]. Pathological beta-range oscillations are detectable on the scalp above the motor cortex[12], directly on the motor cortex[13], or during deep brain stimulation surgery from the basal ganglia[14]. Decreased beta oscillatory power is associated with effective pharmacological and surgical therapy[15,16]. Beta oscillations may be an important biomarker for disease diagnosis and progression, for closed-loop/adaptive deep brain stimulation (DBS)[15], and as a target for neurofeedback training to induce adaptive plasticity in the dysfunctional network[17,18]. To reach these findings, it is common for researchers to selectively choose oscillatory activity with Fourier-based methods that consequently alter the finer temporal features related to disease[19]. Patients at rest do not always exhibit abnormal beta oscillations, and conventional signal processing of resting state cortical beta has failed to reliably identify PD[12,13]. In light of these findings, beta oscillations have not been used reliably for clinical decisions, such as accurate DBS placement or as a trigger for a closed-loop system[15,20,21]. We hypothesize that this may be in part due to subject specificity in the range and shape of activity within the overall beta envelope. In preparation for experiments to be done on PD patients, I tested a processing pipeline aimed at elucidating subject-specific beta changes during movement on healthy subjects as a proof-of-concept for future experiments to be done on PD patients. These findings will be reported later in this thesis.

1.3 Secondary Features More Strongly Associated with Symptoms

Resting state beta oscillations are not sufficiently robust for identifying patient-specific parameters (e.g., frequency, location) nor making clinical decisions. However, beta oscillations are modulated robustly by overt movements. Beta suppression is associated with initiation of planned movements[22], and beta rebound occurs at the termination of a movement[23], or with

stopping a pre-planned movement [24]. Beta activity has therefore been conceptualized as an idling rhythm or promotor processing during the status quo [25–27]. The net inhibition of the BG resulting from increased beta oscillations may permit more accurate choices during difficult decisions [10,28]. Neuroengineering correlates captured from movement may be essential in the characterization of movement related disorders like PD.

2 Chapter 2: Gaze and Subcortical Circuitry in Health and Disease

2.1 Saccadic System and Parkinson's Disease

Eye movements are convenient indicators of basal ganglia (BG) function and eye movement abnormalities are common in Parkinson's Disease (PD) [29–33]. The cortical and subcortical structures involved in the saccadic system require tight regulation in the BG-thalamocortical loop, and degenerates gradually in PD due to decreased dopaminergic innervation from the substantia nigra pars compacta (SNc) [30,31,34,35]. The saccadic system can be evaluated through tasks completed with prosaccades (saccades toward a target), antisaccades (saccades opposite to a cued target), and cognitive tasks involving response inhibition (stop-signal task) [36–39]. Multiple performance metrics of saccades (vigor, latency, corrections) appear to correlate with disease states and various genetic parkinsonisms (PARK1, PARK2, PARK6, PARK9) [32,33,40–42]. Furthermore, electrophysiology metrics derived from cognitive tasks completed with saccades can disentangle various saccade types from unique characteristics in disease states [30,43,44]. The experimental platform reported here uses eye-movements as the model motor system, with simultaneous electroencephalography (EEG). I propose an analysis pipeline and use machine-learning classification to demonstrate that several eye movement features can be faithfully reconstructed from the EEG recordings. The intention is to have a platform that could identify behavioural abnormalities in the parkinsonian state (ie: a PD patient off medication, or with DBS off) and also have the sensitivity to identify the associated EEG abnormalities.

2.1.1 Pathophysiology of Oculomotor Control in PD

The caudate nucleus (CN), STN, substantia nigra pars reticulata (SNr), GPe, and GPi are all major components of the basal ganglia involved in modulating saccadic activity[2,30,34,45,46]. These structures in the basal ganglia receive input from the impaired SNc in PD patients, which limits and dysregulates the SNr inhibition of the superior colliculus. This mechanism results in a reliable correlation between the progression of the parkinsonian disease state and the integrity of the saccadic system[30]. A common medication used to address the depletion of dopamine is a combination therapy of levodopa/carbidopa[47,48], which is adjusted to balance symptom control with side effects. Dopaminergic therapy can affect the saccadic and motor systems in different ways, since the two interrelated systems both rely on BG output. It is important to note, however, that there is ample evidence that PD is a multi-system disorder with the involvement of several brain regions and neurotransmitter pathways other than dopamine[49–52].

Saccade recordings can provide strong clinical applications for probing oculomotor control of the BG. The assertion is supported by a number of saccade studies clarifying the oculomotor deficits in PD, such as hypometria of visually and memory guided saccades, saccadic intrusions, fixation deficits, and impaired combined eye-head tracking[52–56]. Increased inhibition of the superior colliculus (SC) typically correlates with hypometric voluntary saccades, and the dysfunction from frontal BG-SC circuits may cause reduced preoculomotor drive[49,52,57]. Reflexive saccade latency should be unaffected in PD because reflexive saccades are typically generated by direct projections from the parietal cortex onto the SC. However, impaired inhibition of reflexive saccades in PD would provide insight into executive function via antisaccade or countermanding tasks. The antisaccade task paradigm stresses the neural pathways responsible for volitional control and selection, and the STN in the BG-thalamocortical network assures that the increase in probability of one action is facilitated with the decrease in probability of other available options[58]. In addition, errors in antisaccades were shown to be related to freezing of gait (FOG), and increased latency was associated with impaired postural control[29,32,59,60]. Thus, saccade-based experiments could potentially be used to identify and research FOG, which is an important clinical manifestation of PD that has eluded effective therapy[61–64].

2.1.2 Gait and Gaze Network Connectivity

The pathophysiology involved in the FOG has been correlated to frontoparietal and striatal dysfunctions[60,65,66]. Although the behavioural capacities from the cortex and cerebellum could be affected in PD, the mechanism of the BG's dysregulation in fine motor control may be more relevant to FOG in PD. During periods of rest, the GPi and SNr provide tonic GABAergic inhibitory signals over the mesencephalic locomotor region (MLR), pedunculopontine nucleus (PPN), and cuneiform nucleus brainstem structures that control and initiate gait[65,67,68]. The MLR, PPN, and the cuneiform nucleus are also involved in saccade preparation and initiation[56,69,70]. There is evidence suggesting the functional overlap of these nuclei in their involvement with saccade and locomotion[63,65,69,71,72], and the convergence of saccade and limbic signals on single PPN neurons[69].

PD patients with altered connectivity between PPN and frontal regions were likely to present with FOG and antisaccade errors[60,61,64]. Assessing saccades is much simpler than FOG, because of their rapid and ballistic nature, as well as the capability of invoking them in a controlled environment. Compared to prosaccades, antisaccades have stronger oscillatory beta characteristics because antisaccades require driving signals to inhibit reflexive responses[41]. Further supporting the connection between the neural pathways involved in antisaccade and FOG is the evidence that the BG play important roles in effectively switching activity between competing yet complimentary neural networks[62,64]. Saccade metrics require extensive population data to confidently fit a patient's score, but when coupled with electrophysiology, a clearer link between saccades and pathological oscillations can be drawn. We discuss this in greater detail in our experimental design to bring together oculomotor and neural oscillatory data.

2.2 Proposed Saccade-based Stop Signal Task

Modern non-invasive eye-tracking technology features high temporal resolution and addresses its pitfalls (need for head immobilization and errors in pupil tracking) when compared to scleral search coil systems by utilizing advanced algorithms for eye modeling and wearable technology[29,73]. Robust gaze tracking not only expands the utility of PD behavioural tasks when hand-motor movements are unreliable, but also provides accessibility to a wealth of pupillary candidate

biomarkers. For example, pupil reactivity has been shown to be impaired in PD patients[74–76], with pupil modulation being a correlative indicator of task type (prosaccade vs. antisaccade) and cognition[32,41,76]. As an alternative to overt arm movements, saccadic eye movements might be able to modulate beta oscillations. Compared to arm movements, saccadic eye movements are simple ballistic events that are easily quantified and similarly to arm movements, PD patients demonstrate saccade deficits in a probabilistic Go/NoGo (Stop) task and an anti-movement (ie: anti-saccade) task[31,32,44].

The stop signal task is the gold standard for measuring motor response inhibition[36,37,77–82]. Capturing the activation of motor BG pathways using the stop signal task was previously demonstrated on various signal modalities: such as electroencephalography (EEG)[37,78,79], and intraoperatively from the STN[39,80,81,83]. Intraoperative signals from the STN was also capable of capturing the activation of the hyperdirect pathway during BG activation[78]. The executive top-down inhibitory control of action-stopping involved in this task was shown to activate neural pathways analogous to ones in unexpected stopping, such as from unexpected sounds[84], even though the latter does not involve an explicit instruction to engage inhibitory control[85]. This assertion is reflected by previous studies showing unexpected events lead to slowed motor responses and elicit morphologically similar N2/P3 complexes as the ones elicited by stop signals[86–88]. The N2/P3 complex pattern is a event-related potential (ERP) where there is a deflection 200 ms after a stimulus (N2), and a subsequent deflection towards the opposite polarity immediately after, within 300 ms from the stimulus onset (P3). Furthermore, ICA applied to EEG recordings from subjects that performed both the stop signal task and tasks involving unexpected events suggests that both ERP complexes share a common underlying neural generator[80,88]. In the following chapters we outline in detail how ERP complexes measured in our novel saccade task can capture these characteristics without the involvement of hand-motor responses.

A robust experimental paradigm to reliably investigate novel and existing neural correlates of PD disease states is required. We propose a combined EEG-virtual reality (VR) based experimental platform, validate its reliability for research through extensive timing tests, and reproduce results of previous psychophysics tasks by using a custom analysis pipeline capable of real-time feedback.

3 Chapter 3: Description of Experiment

3.1 Sample Size

Seven healthy volunteers participated in the EEG study, and one PD patient participated in the intracranial study during DBS surgery.

3.2 Task Platform Outcomes

Saccade-based tasks can modulate neural oscillations in the BG thalamocortical network, and it is hypothesized that the recorded neural activity can be used for analysis with pathological oscillations recorded during the resting state. EEG and eye-tracking were used to measure parameters from currently known neural correlates of saccade in Parkinson's Disease [29–33].

Consistent failure to maintain fixation was an indicator of PD [32]. We have tested this system in healthy participants and have established an analysis pipeline to identify neural correlates of saccadic performance (see Chapter 3). Specifically, common spatial patterns (CSP) will identify neural signals that discriminate Go vs Stop trials and future applications in successful vs unsuccessful stopping [89].

3.3 Data Collection

At the beginning of the session, the participant's head was measured to determine the correct placement of the EEG cap based on standard guidelines (international 10-20 system) [90]. For example, measuring the midpoint between the nasion and inion shows the position of CZ, which marks the centre of the scalp. The reference electrode was placed on the patient's mastoid process and secured by medical tape. Electrode gel was carefully applied via the wells of each electrode, and the application process continued until every electrode had a recorded impedance of less than 5 kΩ.

Participants donned a head-mounted virtual reality display with built-in eye tracker. After a brief eye-tracking calibration period, participants were asked to perform a stop signal task with prosaccade or antisaccade cues (Figure 1). In each trial, participants were instructed to maintain gaze on a central fixation point through cue and target presentations until cued to

make a prosaccade towards or antisaccade away from a target.

3.3.1 Lab Streaming Layer

The lab streaming layer (LSL) is a system for the unified collection of measurement time series in research experiments that handles both the networking, time-synchronization, and centralized collection and recording of the data[91]. LSL has been used in EEG-BCI experiments for its near-real-time data access for feedback[92,93]. This experimental platform uses tools built on top of the LSL library: LabRecorder provides the list of available sources and records to disk, and LSL software required for interfacing with the acquisition hardware described in the subsequent sections (EEG, Pupil-Labs Eye-Tracking, Unity3D, OpenVR).

3.3.2 Virtual Reality for Research

Virtual Reality (VR) is a computer-simulated environment that provides an immersive environment for the user. VR is capable of stimulating many senses that traditional user interfaces cannot[94,95], such as combinations of vision, hearing, touch and sometimes even smell[94]. Recently, VR has been advantageous for many areas of medicine, such as medical training and therapy for physicians and patients[94], and brain-computer interface (BCI) research. This is because of its flexibility in manipulating virtual environments (i.e.: placing the subject in inaccessible locations), low latency in processing events (switching states without breaking immersion), and high fidelity in the presentation and processing of visual information. Due to the high computational demands of VR and various signal or interfacing sources in neurophysiology (eye-tracking), it is uncertain whether these tools are robust enough in temporal precision and in supporting a neurophysiology experimental platform.

3.3.3 Platform Reliability Design

The suggested experimental platform requires low latency and jitter to capture important details and to obtain high confidence for determining causation of meaningful events, such as measuring electrophysiological responses to different sensory stimuli. Task designs like these typically present a sequence of visual and auditory events. It is important to determine when the events occur, when the subject responds, when the neurophysiological events occur, and

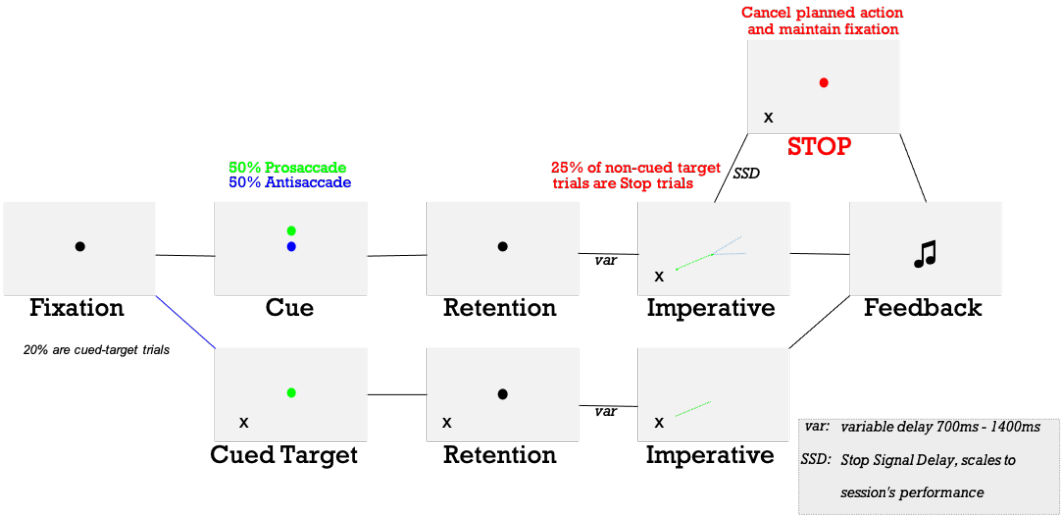

Figure 1: Task schematic for the Stop Signal Task with cued prosaccade and antisaccade. The typical trial would follow the phases: fixation, cue, retention, imperative, feedback. The imperative phase was when the fixation disappeared (and simultaneously a target appearing), indicating the subject to make a saccade based on the cue's task condition (prosaccade or antisaccade). In a small number of trials, a red stop cue would appear very shortly after the fixation point disappeared, prompting the subject to withhold their planned saccade and maintain central fixation. The cued target scenario was the same as the typical phase, but with the target displayed throughout the entire trial. This scenario would be the easiest and was the control, because the target location was revealed and the subject would have to wait until imperative to make a saccade.

whether these occurrences are consistent. Although the goal is to minimize latency and jitter, the minimum requirements are elucidated from previous evoked potential EEG studies: visual evoked potentials are thought to occur at a mean latency of 100 ms[96–98], and auditory evoked potentials vary based on the propagation of related brain regions. These include the late cortical auditory evoked potentials (range between 50-500 ms[99]), and the objective predictor N1-P2 complex (at approximately 100 ms[100]). More details are outlined in the appendix of this thesis.

3.4 Proposed Stop Signal Task with Prosaccade, Antisaccade, and Sustained Cued Saccades

At the beginning of each trial, the gating phase prevents trial progression until the subject maintains fixation on the fixation point for more than 400 ms. The subsequent cue state transiently changes the colour of the fixation point to either green or blue for 800 ms, instructing

the subject to prepare for either a prosaccade or antisaccade when the fixation point disappears. After the cue phase ends, the fixation point was restored to a neutral colour and a variable delay period followed, from 600 ms to 1400 ms. The imperative phase followed the variable delay period, and the fixation point relocated to either the left or right to prompt the subject to make a saccade toward or away from it. A Stop trial occurred on 20% of trials, where a red fixation point would appear shortly after the imperative phase to instruct the subject to interrupt their planned saccade and maintain central fixation. The stop signal delay (SSD) was the metric for the delay until the red fixation point appears, and the SSD would adjust in a stepwise manner $\pm$ 22 ms depending on the subject's performance. This dynamic adjustment was intended to reinforce subject immersion throughout the experiment, increasing the difficulty of the stop trials by providing less time for the subjects to cancel their planned movement. The difficulty of the task was important to elicit a strong inhibitory response.

The participants were informed that cued trials could never result in a stop trial. During this trial, a target appears during the cued phase and remains visible until the central fixation point disappears. These cued trials were used to probe for motor planning, and could be used to isolate positional and eye movement artifacts if necessary.

4 Chapter 4: Analysis Methods Literature

4.1 EEG Equipment

Continuous EEG was DC-recorded using the g-Tec USBamp DC amplifier LSL software. The sampling rate was 500 Hz with 16-bit resolution, and the EEG was digitally bandpass filtered 0.1 Hz to 60 Hz.

All electrodes were online referenced at CZ and grounded at the subject's mastoid process. Electrode impedance was kept below 5 kΩ.

4.2 EEG Pre-processing and Filtering

Filtering signals helps to facilitate the extraction of relevant biophysical signals, and using filters properly can prevent the occurrence of signal distortions. The first step of pre-processing

usually involves applying a common average reference (CAR). CAR is computationally simple and can eliminate uncorrelated random noise with zero mean, for example thermal noise. Previous EEG research had shown that CAR is beneficial at identifying small signal sources in very noisy recordings[101] and operates by computing the average of all recordings on every electrode site and uses them as a reference. The result would yield the signal/noise that was common to all sites (60 Hz noise). The subsequent filtering procedures are ubiquitous in electrophysiology research, but choosing the correct filter design and parameters can prevent poor signal-to-noise ratio and the introduction of artifacts that affect the interpretation of the results[102]. The finite impulse response (FIR) filter is a high fidelity and stable filter, and accepts an additional parameter called the roll-off. The roll-off is the slope of the magnitude response between the pass-band and stop-band (transition band)[102]. Steep roll-off parameters can separate signal and noise components in adjacent frequency bands better than wider parameters, but can potentially produce stronger signal distortions and worse smearing and artifacts[102]. Low frequency noise is the most common source of noise in electrophysiological recordings, and steep roll-offs are often required for high-pass filtering.

The NeuroPype pre-processing meta-node first imported the XDF file and checked the integrity of the time-stamps and data structure (EEG channels and their location). The data was re-referenced using the CAR technique. An FIR filter was used as a high-pass filter to remove low noise frequencies, with 0.1 Hz and 0.5 Hz specified as the roll-off curve. The high-pass filtered data was placed into an artifact removal node, designed to remove various kinds of high-amplitude artifacts identified based on a specified threshold. This filter aided in the removal of movement artifacts, such as blinking and muscle activity, and was capable of handling high amplitude sensor glitches or electromagnetic interference.

4.3 Signal Processing and Feature Extraction

The signal processing pipeline was executed on a per subject basis for extracting subject-specific beta peaks (Figure 2). The task modulating component from independent component analysis (ICA) was manually determined based on topography and event related potentials (ERP) that most closely resemble previous literature.

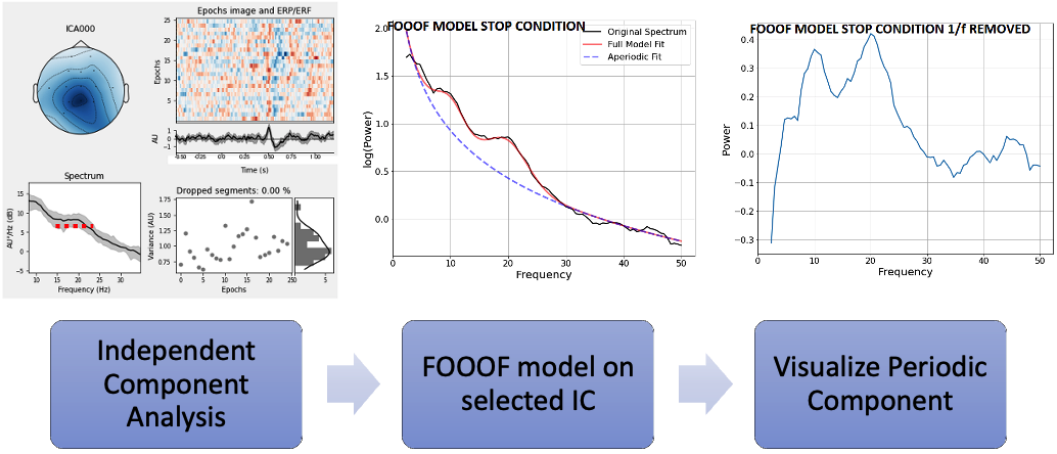

Figure 2: Overview of process for retrieving subject specific beta peaks. The task modulating component was manually selected per subject, and its spatial filter was applied to the session timeseries. The power spectral density was computed from the timeseries, and FOOOF modelling was fitted. After subtraction of the aperiodic component, the periodic components could be visualized through peaks, and automatically extracted via code.

4.3.1 Event Related Potentials

Event-related potentials are EEG changes to specific events or stimuli time-locked to sensory, motor, or cognitive events, which represent the temporal signature of macroscopic electrical activity [103]. ERPs reflect the summed activity of postsynaptic potentials produced when similarly oriented cortical pyramidal neurons fire in synchrony [104]. ERPs generally provide information about sensory and cognitive states in the brain, depending on the amplitude of the ERP and its latency from stimulus onset.

The ERP was calculated for each subject to ensure that the novel experimental platform was functioning as expected. Strong evoked potentials were expected to be identifiable during the imperative phase if the event was processed with sufficient temporal precision. Each imperative phase per trial always began with the disappearance of the fixation point, and a resulting ERP would verify that biological signals were recorded in each session.

4.3.2 Independent Component Analysis

ICA is an established technique in EEG processing, primarily used in data decomposition and identification of neural activity [105]. The main assumption is that the recording channels

contain a mixture of independent source components. Thus, the overall goal of ICA is to infer the independent factors (sources) using test observations (mixtures)[106]. It is important to note that this algorithm, in the context of machine learning (discussed in subsequent sections), is unsupervised (extracted components are unlabeled) and thus requires the researcher to manually determine their neural component. The ICA paradigm of vector $X \epsilon \mathbf{R}$:

$$X = AS \tag{1}$$

where X can be expressed as a non-singular linear transformation of d mutually independent latent factors $S_1, ..., S_d$ and A as the mixing matrix. Given that the sources are mutually independent, ICA can be achieved from the source estimate matrix U by estimating the de-mixing matrix W:

$$U = WX \tag{2}$$

There are many ways to calculate the de-mixing matrix estimation, such as minimizing mutual information or maximizing likelihood estimation[107,108]. One methodology that alleviates the burden of tuning parameters (i.e.: violations of parametric statistics) and entropy is nonparametric maximum likelihood:

$$log|detW| + (\frac{1}{n}) \sum_{i=1}^{n} \sum_{j=1}^{d} log f_j(w_j^T x_i) \tag{3}$$

where W is estimated by maximizing the likelihood over all dxd matrices and univariate densities $f_1, ..., f_d$ of the latent factors. We used the python MNE toolbox which uses algorithms adapted for neural signal processing applications[109]. The time complexity of this algorithm is $O(n * m)$ where n is the number of samples and m is the number of iterations. As the number of samples collected increases, the amount of time required to complete this algorithm increases linearly.

4.3.3 Determination of Task Modulating Component using ICA

After ICA was computed for the source components on the continuous session recording, the components were visualized in time-series time-locked to the imperative phase. The independent component (IC) topologies that represent artifacts or non-neural features were excluded, and the

component that contained the event-related synchronization or desynchronization (ERS/ERD) features was kept (Figure 2). ERS or ERD were observations of increases or decreases in signal amplitude in response to a particular stimulus, respectively. The N2/P3 complex introduced previously was an example of two ERS and ERD events in quick succession of each other in response to stimuli. If the IC contained ERS followed by ERD during the time-window of a trial, then this IC may modulate with the task condition[85,86]. The continuous data session was transformed with the IC of interest (as described above) for further analysis.

4.3.4 Fitting Oscillations and One Over F

Fitting Oscillations and One Over F (FOOOF) is a specialized modelling tool for parameterizing neural power spectra[110]. The power spectrum of a given segment of neural data can be illustrated as a combination of two functional components: 1/f aperiodic component, and oscillatory component. In PD the oscillations in the beta range (13-30Hz) have been shown to be physiologically significant in representing the disease state[3,10,12,14,19,20,27,37,111–116]; however, due to the large range of the beta band, features identified in this manner may not always accurately depict the pathological state.

FOOOF provides an automated approach for measuring the oscillatory contribution in the provided power spectrum via identifying peaks characterized by their specific centre frequency, power, and bandwidth. This involves the following successive reconstructions of the aperiodic and periodic components. First, the initial aperiodic component was fitted on the given power spectra, and then subtracted out to visualize peaks. Second, the periodic components were determined by fitting gaussian functions to determine the locations of possible peaks. Lastly, the peak functions were subtracted out of the initial power spectra to reconstruct the final aperiodic curve. The variance and goodness-of-fit could be calculated by comparing the initial aperiodic curve with the final aperiodic curve. Peaks identified in the beta range would show task-specific narrow-band modulation. In addition, the aperiodic component may be utilized in across-session comparisons, suggesting a subject-unique aperiodic component[117]. The time complexity of this algorithm increases in a squared manner as the number of samples increases $O(n^2)$.

The FOOOF algorithm was applied to each subject's task-related IC to compute a spectral model for each subject as per the task conditions. The algorithm extracted probable peaks,

represented by its centre frequency, broadband width, and power. After the subtraction of the aperiodic component, the peaks could be better visualized and quantified (Figure 2).

4.4 Machine Learning and Classification

Machine learning uses predictive modeling to find unknown values, and identifies relationships between the data that describe characteristics (features) and the values we want to predict (labels). For example, consider

$$y = f([x_1, x_2, x_3, ..., x_n] \tag{4}$$

where y represents the label we want to predict and x represents the features the model uses to predict it. The overall goal is to train a model that performs some calculations to the x values so that they produce result y. Machine learning has been used extensively in electrophysiology, such as decoding the alphabet for typing[118–120], decoding sleep disorders from sleep states[121], and so on.

In human neural data, two major problems for pattern recognition and machine learning are the nonstationarity and inherent day-to-day variability of neural signals[103], even when recorded under seemingly identical experimental conditions. In addition, various thoughts, stresses, and boredom may introduce task-unrelated neural activity that may contribute further to the variability of session recordings. Therefore, it is important to ensure that the trained model can be generalized for adapting to future recordings while maintaining sensitivity for subject-specific states. We propose that the above described FOOOF and ICA pipeline would yield powerful indicators of subject-specific parameters, and the extracted subject-specific beta band would guide the modeling process for prioritizing neural features related to response inhibition.

4.4.1 Common Spatial Patterns

Common Spatial Patterns (CSP) is a machine learning estimator comprising four progressive stages of EEG processing: band-pass filtering, spatial filtering with the CSP algorithm, CSP feature selection, and classification of the selected CSP features. The CSP algorithm was designed to find spatial filters that maximize variance for one class and minimize variance for the other class at the same time[122–124]. X_H and X_F denote the preprocessed EEG matrices under two

different classes, with dimensions N x T, where N is the number of channels and T is the number of samples per channel. Below is the normalized spatial covariance of the EEG:

$$R_H = \frac{X_H X_H^T}{trace(X_H X_H^T)} \qquad R_F = \frac{X_F X_F^T}{trace(X_F X_F^T)} \tag{5}$$

X^T is the transpose of X and $trace(A)$ computes the sum of the diagonal elements of A. The averaged normalized covariance $\overline{R_H}$ and $\overline{R_F}$ are calculated by averaging over all the trials of each group. Below is the spatial covariance where U_0 is the matrix of eigenvectors and Σ is the diagonal matrix of eigenvalues:

$$R = \overline{R_H} + \overline{R_F} = U_0 \Sigma U_0^T \tag{6}$$

Both conditions share common eigenvectors and the sum of the corresponding eigenvalues for the two matrices will always be one:

$$\Sigma_H + \Sigma_F = I \tag{7}$$

Transforming the EEG matrices onto the eigenvectors corresponding to the largest eigenvalues in Σ_H and Σ_F is optimal for separating variance in the two signal matrices; the eigenvectors with the largest eigenvalues for group H have the smallest eigenvalues for group F and vice versa. Each trial was labeled as a Go or Stop trial, where Go includes trials containing the presence of a saccade (prosaccade or antisaccade), and Stop for trials containing the stop signal. The Go and Stop labels served as the two classes that CSP attempted to discriminate from the trials. The output of CSP was a pair of spatial filters: one that maximizes the variance for one class and minimizes variance for the other, and vice versa for the reverse condition. Spatial patterns of the corresponding filters were visualized via topographical plots. These topologies are visualizations of the constructed model and are important when analyzing the regions of the scalp that contributed most to the model (source localization).

In this study, validating the placement of the weights was important to detect overfitting to artefacts or noise. For example, the model could be fitted to the presence of a saccade, and as a saccade detector this would have perfect classification accuracy for detecting Go vs Stop trials. By having more weight towards the centre region of the scalp, and avoiding patterns most

commonly associated with non-neural sources, the model can be influenced to detect features coming from neural sources. Since the previous ICA and FOOOF pipeline revealed oscillatory characteristics that contributed to the completion of this task, this narrow band was used to guide the CSP to differentiate between the two task conditions properly.

4.4.2 Classification and Cross Validation

Classification is a form of machine learning in which a model is trained to predict the category that an item belongs to. In supervised methods, the dataset can be partitioned into 3 sets (training, validation, testing) to ensure that the trained model can generalize and avoid overfitting. The model is trained on a dataset with labeled features (training set), estimated by tuning hyperparameters (validation set), and evaluated by whether the model can successfully label new input signals (testing set). To determine a classification technique suitable for our dataset, cross validation was conducted to maximize the amount of data considered in training.

Cross validation is a resampling procedure used to evaluate machine learning models and access how the model will perform for an independent test dataset. Traditionally, a segment of the dataset would be sectioned off for testing and the rest for training. This introduces theoretical problems in time series data, such as temporal evolutionary effects and inability to make full use of the data[125]. There are various methods in cross validation to address this, but for the scope of this thesis each model trained was shuffled with a random seed[126], and passed into scikit-learn's cross validation pipeline[127]. This step allowed the full sampling of the datasets and provided the appropriate accuracy and error metrics required to make decisions on which model (and modelling parameters) to choose for the classification pipeline.

Hyperparameter optimization was conducted during model consideration to search for the best performing parameters to pass into each model. This was prototyped locally with scikit-learn's grid search, and automatically fulfilled with AutoML for systematically testing various models per subject[128,129]. Below is an overview of some of the models considered and literature surrounding the model's classification techniques.

Support vector machine (SVM) provides a classification learning model, and assigns labels to objects from learning by example[130,131]. In linear modelling two main steps are involved: the mapping of the data domain into a response set and the dividing of the data domain. Consider the

following straight line equation on the data domain that will divide the data into two subdomains D_1 and D_2:

$$wx' + \gamma = 0 \tag{8}$$

where w, x' and γ are parameterized values determined by optimizing how well D_1 can be distinguished from D_2 (typically by optimizing the distance).

$$D_1 = \{x : wx' + \gamma <= 0\} \tag{9}$$

$$D_2 = \{x : wx' + \gamma > 0\} \tag{10}$$

The points that fall in the subdomains are labeled 1 for subdomain D_1 and -1 for subdomain D_2. Two straight lines can define the parameterization objective for defining the boundaries between the D_1 and D_2:

$$wx' + \gamma = 1, x \epsilon D_1 \tag{11}$$

$$wx' + \gamma = 1, x \epsilon D_2 \tag{12}$$

For higher dimensional spaces, the lines from the parameterization objectives will solve for hyperplanes which will be used to define the boundaries between the classes of data. The optimization of these parameters was handled by the algorithm toolbox and is primarily accomplished by maximizing the distance to the closest data points from both classes [130–132], as well as applying the proper cost functions [133]. In addition, features used to infer the hyperplane are not typically raw data, and are often derivative data resulting from interpolation [132]. This is a common theme in the engineering of machine learning algorithms and pipelines: to provide outputs guided by statistically relevant methodologies for researchers to draw conclusions from.

```
from mne.decoding import CSP
from sklearn.model_selection import train_test_split
from sklearn.svm import SVC

cv = ShuffleSplit(10, test_size=0.3, random_state=42)  # 30% for testing
csp = CSP(n_components=2, reg=None, log=True, norm_trace=False)
model = SVC()
```

```
clf = Pipeline([('CSP', csp), ('SVC', model)])
scores = cross_val_score(clf, epochs_data_train, labels, cv=cv, n_jobs=1)


```

Listing 1: Sample early stages of pipeline design for CSP estimation and SVM classification. The *epochs_data_train* variable contains Go and Stop trials and *labels* contain an array indexed for identifying Go or Stop trials. For more details refer to the appendix and code repository.

One of the main advantages of constructing the classification pipeline in this way was that testing a different model would simply be redefining the model variable. The random forest (RF) classifier was chosen to compare with the classification results from SVM. The random forest classifier is an ensemble approach for classification, in which many classifiers are generated and their results are combined for greater classification performance[134,135]. Implementations of the algorithm typically involve bagging and is used in tandem with random feature selection[136]. Bagging (bootstrap aggregation) in decision trees involves the process of sampling with replacement and then averaging the regression trees. Given a training set $X = x_1, ..., x_n$ with responses $Y = y_1, ..., y_n$, regression tree f_b is trained on X_b and Y_b. Predictions for unseen samples x' could be calculated from averaging the predictions from all the individual regression trees on x':

$$\hat{f} = \frac{1}{B} \sum_{b=1}^{B} f_b(x') \tag{13}$$

for $b = 1, ..., B$ bagging B times. This method has been extensively shown to reduce variance by training on different samples of the data and using a random subset of features[136].

Each of these constructed classifiers could be evaluated in many ways. To highlight the importance of using subject-specific parameters, the classifiers created for default beta and subject-specific beta were scored using cross validation, visualized with the receiver operating characteristic (ROC) curve, and summarized with a statistical report (F1, precision, recall). These were compared side-by-side to see statistical relevance for guiding the model with specific parameters. A practical application in machine learning is to deploy the model for inferencing not only on testing data, but also on data recorded at a separate time for monitoring data drift.

```
from mne.decoding import CSP
```

```
from sklearn.pipeline import Pipeline
from sklearn.ensemble import RandomForestClassifier
model = RandomForestClassifier()
clf = Pipeline([('CSP', CSP()),
                ('RandomForest', model)])
scores = cross_val_score(clf, epochs_data_train, labels,
                         cv=ShuffleSplit(20, test_size=0.3), n_jobs=1)
```

Listing 2: Sample pseudocode for assembling the RandomForest model, cross validation method, and pipeline parameters to calculate classification accuracy.

```
# Note: This is simplified pseudocode
    for train_idx, test_idx in cv.split(epochs, labels):
        y_train, y_test = labels[train_idx], labels[test_idx]

        # Fit classifier
        clf.fit(epochs[train_idx], y_train)

        predictions[test_idx] = clf.predict(epochs[test_idx])
        auc_scores[test_idx] = roc_auc_score(y_test, clf.predict_proba(epochs[
    test_idx])[:, -1], multi_class='ovr')

        # Running classifier: Trained CSP estimator transforms testing segments
        score_this_window = []
        for n in w_start:
            # Note: Last index is n_samples in trial (ie: 851).
            # This loop slides across n:(n+window)
            X_test = clf['CSP'].transform(epochs[test_idx][:,:,n:(n+w_length)])
            X_test = Vectorizer().fit_transform(X_test)
            X_test = MinMaxScaler().fit_transform(X_test)
            score_this_window.append(clf['Model'].score(X_test, y_train))
        sliding_window_scores.append(score_this_window)
```

Listing 3: Sample code for scoring time windows. The trials were split into training and testing sets. For every trial, the CSP estimator and the RF model were trained and subsequently scored in a time-window fashion on a trial from the testing set. All the scores from the testing trials were averaged at their respective time-windows, and the score over time was plotted.

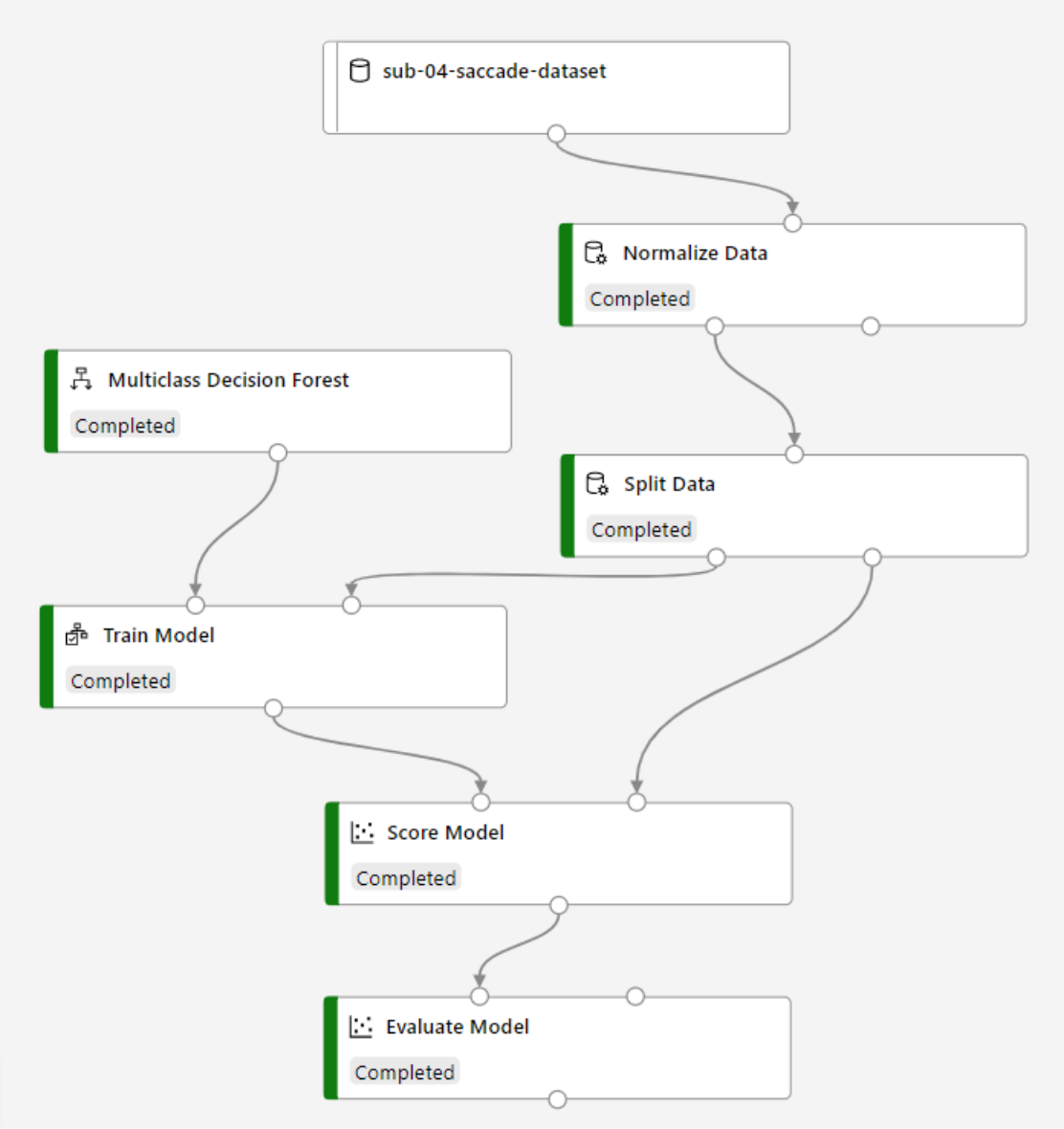

Figure 3: Schematic for the initial steps of training the model for inference using Azure Machine Learning Studio Designer.

4.4.3 Deploying models for inference and monitoring drift over time

In machine learning, inferencing refers to the use of a trained model to predict labels for new data on which the model has not been trained. It is important to verify the utility of this framework for future use cases, even if techniques used throughout the training process were best

practices for ensuring that the model could be generalized. In this project's future objectives, this could involve tuning the model during follow-up patient visits and real-time feature mapping of PD progression. In this pilot study with healthy subjects, this type of monitoring was prototyped using a follow-up session recording given a known amount of time between the two recordings, as data drift in regards to time is also a metric that can be modeled. Subjects volunteered to complete this task again after the first round of data collection. The models trained for

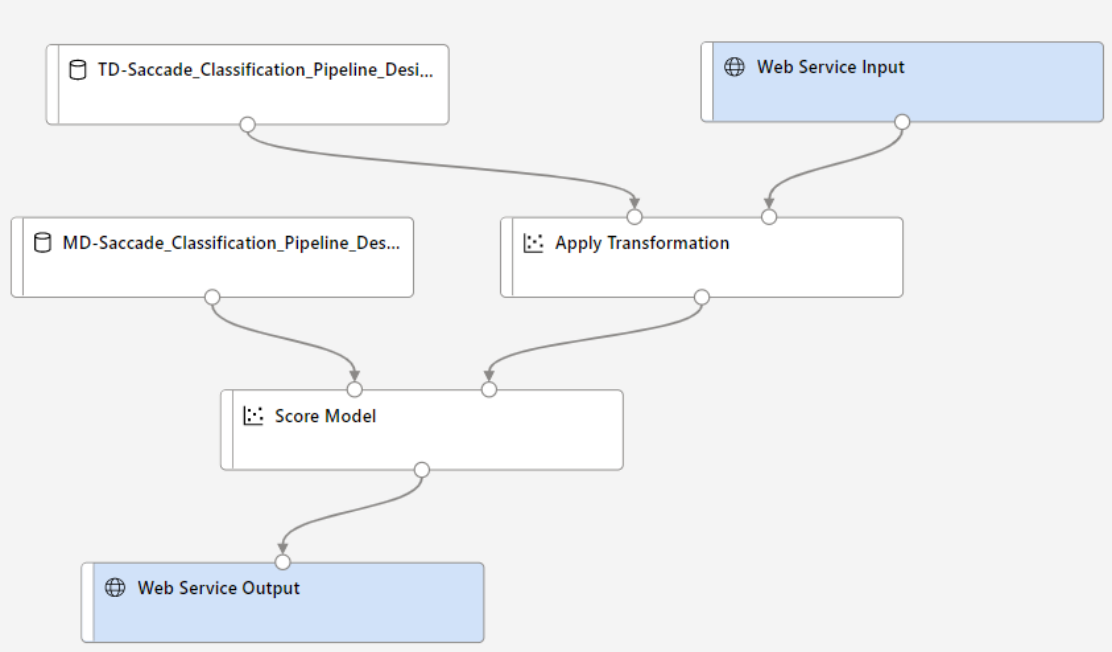

Figure 4: Schematic for the real-time inference pipeline generated from the designer.

differentiating between Go vs Stop trials and between saccade types were constructed to work in Azure Machine Learning Studio, as visualized in the designer in Figure 3. After training, the model was registered and deployed on an Azure Kubernetes Service (AKS) cluster, known for its real-time capabilities and high availability (continuous usage and robust reliability) in enterprise applications[137]. A schematic of how this endpoint was consumed is shown in Figure 4, where the naive data came from the Web Service Input and the prediction (Go vs Stop) would be printed from the Web Service Output. The AKS cluster was chosen for its capability of scaling its resources depending on the demands of the machine learning pipeline, which may be important for more resource intensive classifiers and future applications in deep learning. The

monitoring feature was registered in combination with this cluster to show possible drift between the baseline and target datasets.

After deployment, the endpoint was consumed with a sample notebook containing random trials sampled from the subject's second recording. The model evaluated the trials in real-time and provided its predictions. These predictions and performance metrics were logged. The second recording was used for the performance metrics, which include the confusion matrix, F1 score, and recall.

5 Chapter 5: Results

Timings of each event were recorded and timestamped during each trial. Events included stimulus presentation, object selection, and phase transition (Figure 1). Parallel streams of data event markers that were pushed onto the data (LSL) stream were used to synchronize the EEG and eye-tracking data (Table 4). Each stream contained a time axis respective to the data source's sampling rate, and alignment was possible with LSL's integrated software clock.

5.1 Proposed Stop Signal Task with Cued Prosaccade and Antisaccade

Participants in this study completed the task after a brief instructional and trial period, while the task's difficulty scaled to their performance via the stop signal delay (SSD) measure. Each recording session's trials were segmented into timeseries beginning 500 ms before the fixation disappeared and ending 1200 ms afterwards. The average of all trials for a subject would show an event-related potential (ERP), to show that electrical changes recorded were consistent across every trial and that random events would appear much smaller in magnitude. The ERP in the context of this task was expected to show a N2/P3 complex pattern, where N2 was a deflection in potential 200 ms after a stimulus, and P3 a deflection towards the opposite polarity immediately after. In the stop signal task, the stimulus would be a red stop cue that appeared around 150-200ms after the fixation point disappeared (0.0 mark in subsequent figures), and the N2 would be expected to appear at 0.4s using this time scale.

5.2 Event Related Changes after Imperative Phase

In the stop trial condition, all subjects had event related potentials detailing the N2/P3 complex, typically across the CZ and PZ electrodes (Figure 5). Each trial involved in the average timeseries shown was time-locked at the imperative phase marked at 0 seconds, or the vertical black line. The stop signal stimulus varied across subjects, but on average occurred 150 ms after the imperative. This was reflected in the slight variation in the onset of the N2/P3 complex among the subjects.

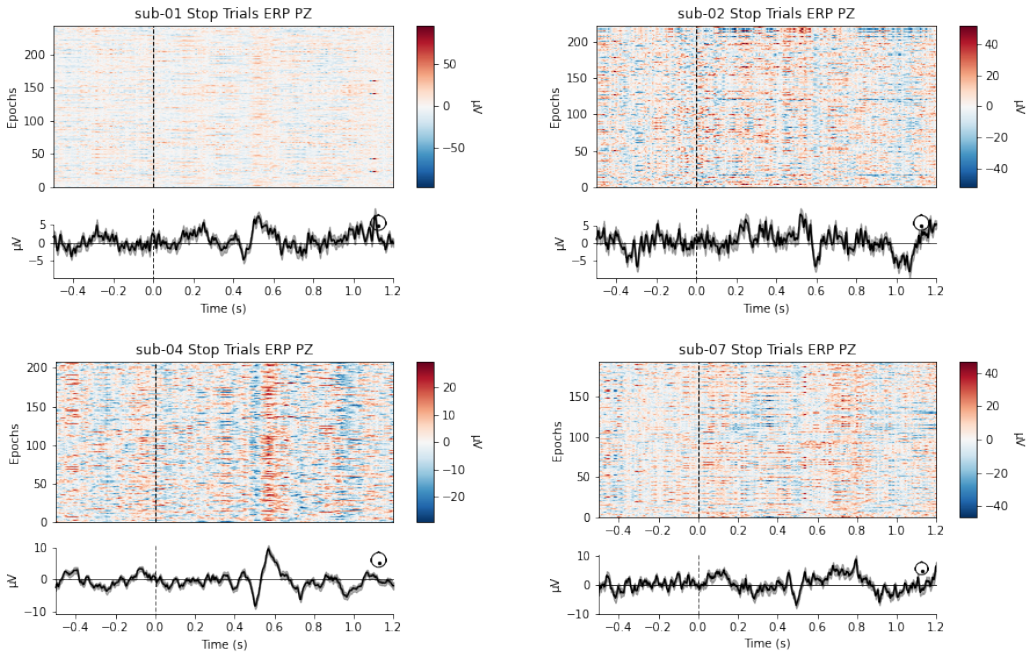

Figure 5: ERP from selected participants during the stop trial condition. The averaged epochs were baseline corrected and underwent NeuroPype's preprocessing pipeline. The 0.0 position marked the event when the fixation point disappeared, which indicated the imperative to make a saccade. All epochs were time-locked to the imperative event.

5.2.1 Event Related Spectral Perturbation

The event-related spectral perturbation (ERSP) were computed for all subjects to show how ranges in frequency (Hz) increase or decrease in power throughout the timespan of a trial. Compared to ERP, the ERSP would show finer detail in which frequencies contributed most to the deflections that occurred by referring to the time domain. The ERSP for each subject showed the average relative onset of phase synchrony in response to the imperative phase timelocked at 0 (Figure 6). The average spectrograms during the trial of four participants is shown in Figure 6, demonstrating gradually increased power in the lower frequencies starting at 250 ms after the imperative phase.

5.3 Event Related Potential Isolated from ICA on Stop Trials

ICA was trained on the continuous segment of the recording across all recording electrodes to determine statistically independent components captured in the timespan of the recording. The

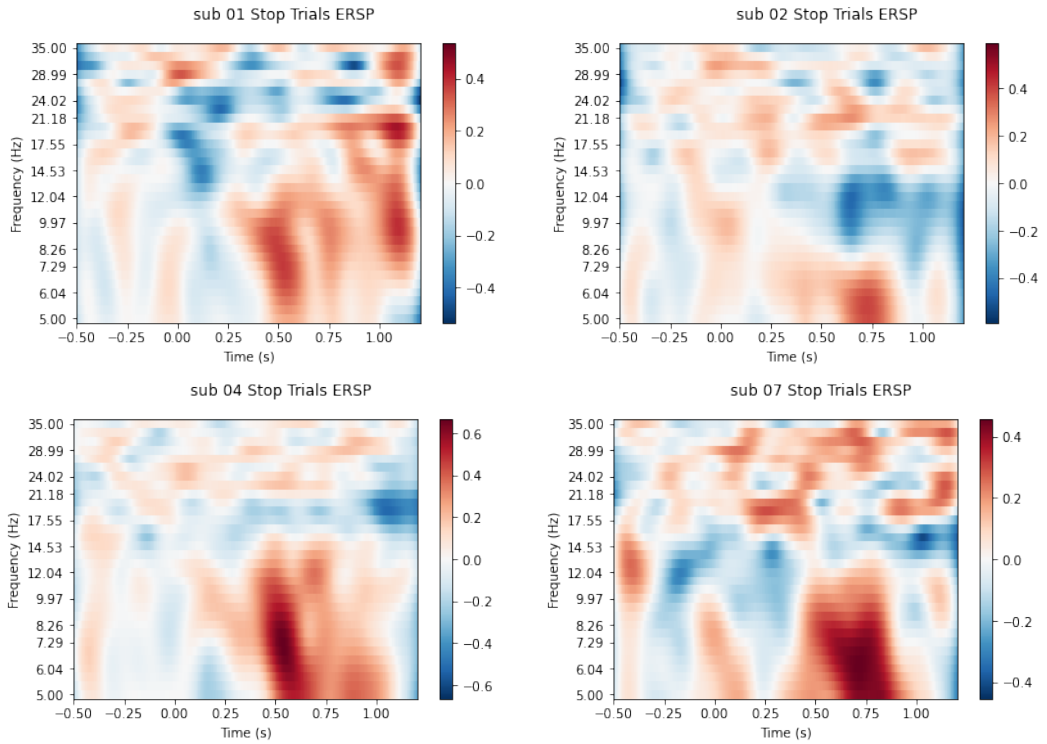

Figure 6: The ERSP throughout the trial from selected participants, where the 0.00s denoted the period when the fixation point disappeared. The trials used to construct these plots were successful stop trials from each subject, to show maximal shading in the frequency components involved in completing the stop action.

algorithm was unsupervised because there was no experimenter bias indicating when trials were started or paused. The graphs displayed were trial segments transformed by the components in the trained ICA algorithm, to see whether the components were capable of capturing the response inhibition brought out by the stop condition trial.

The number of sources was set to the number of channels that were kept after the preprocessing phase. Stop trial-related ERPs were identified from one of the first 8 IC's for all subjects by visualizing each component's event-related potentials that were time-locked at the imperative phase. Every subject had topologies that showed increased weights across the CZ and PZ source locations, and N2/P3 complexes at around 500ms after the imperative phase (Figure 7).

In the bottom left power spectra, a time-frequency representation was shown for the electric activity captured in the timespan of the trial after being transformed by the trained IC. Background noise is characterized by an aperiodic or 1/f pattern, and a slight bump would indicate

the presence of increased power in that frequency range. Every subject had increased power (hill-shaped features) in the alpha (8-13 Hz) and beta (13-30 Hz) range. The epochs for the shown IC for each subject were passed into the FOOOF algorithm.

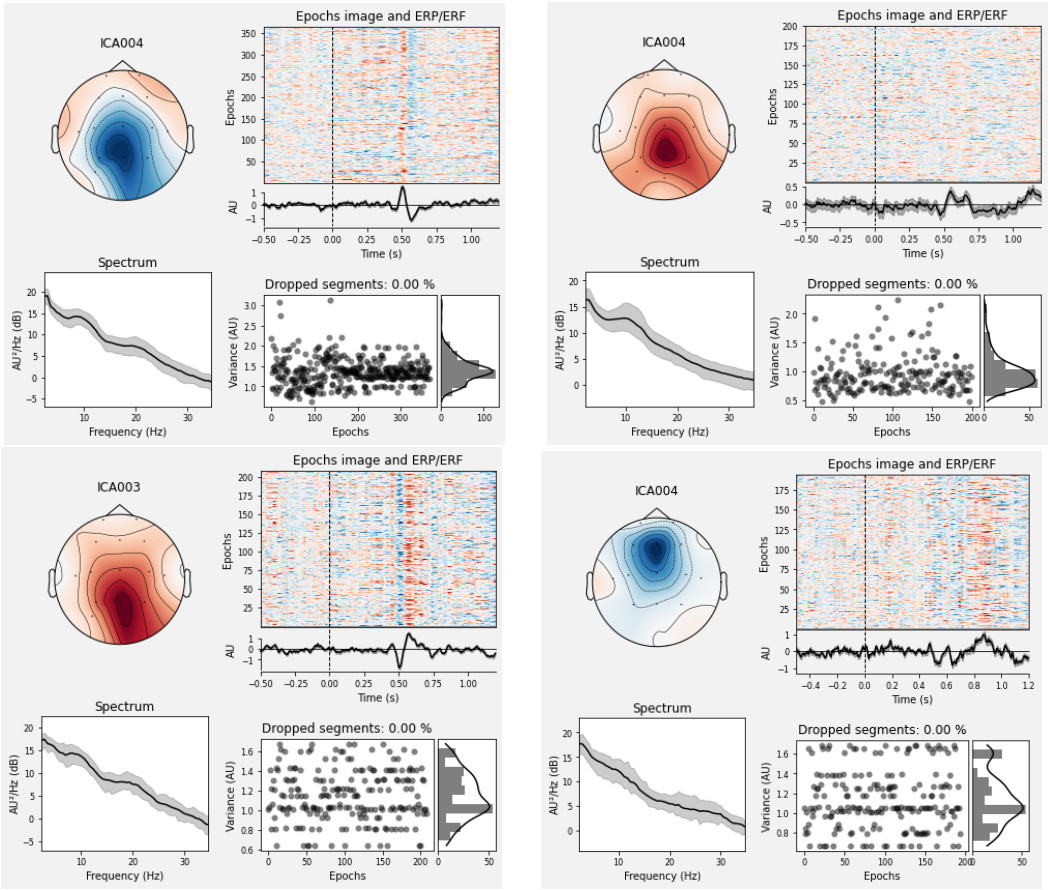

Figure 7: The selected IC profile for each subject, showing the overall topology, the ERP and ERSP characteristics, the time-frequency spectrum, and variance distribution.

5.4 FOOOF modeling showed unique narrow band peaks

The power spectra transformed from each subject's IC were fed as inputs to the FOOOF algorithm, to achieve more granular precision of the frequency ranges that had increased power. The FOOOF models constructed for every subject's IC extracted a narrow band of beta activity, and typically contained a peak in the alpha range (Table 1). For each subject, the beta band automatically determined by the FOOOF algorithm was more narrow than the broad beta range.

The peak characteristics were unique in each subject, with varying central frequency, bandwidth, and power (Figure 9).

Subject	Alpha Range (Hz)	Error of fit	R^2 Score	IC	Beta Range
1	(11, 13)	0.0336	0.9718	4	(29, 32)
2	(9, 13)	0.0273	0.9949	4	(15, 20)
3	None	0.0285	0.9775	3	(28, 32)
4	(7, 10)	0.0211	0.9962	3	(13, 19)
5	(5, 9)	0.0416	0.9398	1	(23, 28)
6	(7, 13)	0.0146	0.9958	8	(17, 24)
7	(8, 12)	0.0141	0.9982	4	(20, 25)

Table 1: Peak parameters extracted from FOOOF model fit for every subject using spectrograms transformed by their selected IC. Alpha ranges were extracted for every subject except subject 3, and the narrow beta peak with the highest power was selected for subjects that had more than one beta peak.

5.5 FOOOF detected additional oscillatory features on signals de-mixed by ICA compared to raw signals

In the previous figures with ERP and ERSP (Figure 5 and Figure 6), these patterns were extracted raw from the session recording, named pre-ICA. High amplitude influence from the lower frequencies could mask finer contributions from the higher frequency ranges, so a comparison between pre-ICA and subject IC was conducted. The power spectra between the data pre-ICA and after ICA showed differences in the beta range (Figure 8). After subtraction of the aperiodic component, the detectability of the beta peaks appeared to be more enhanced in the FOOOF analysis of the ICA condition (Figure 9) compared to the FOOOF analysis of the raw session recording. This increased presence of peaks detectable in the FOOOF algorithm was observed in all subjects (Figure 9). Increased detection of peaks was generally interpreted as narrow frequency ranges of synchronized activity in a hill-shaped pattern. For sub-06, the subject-specific task-modulating component revealed an alpha peak, and for sub-01 this method revealed both the subject-specific alpha and beta peaks that were absent in the raw data.

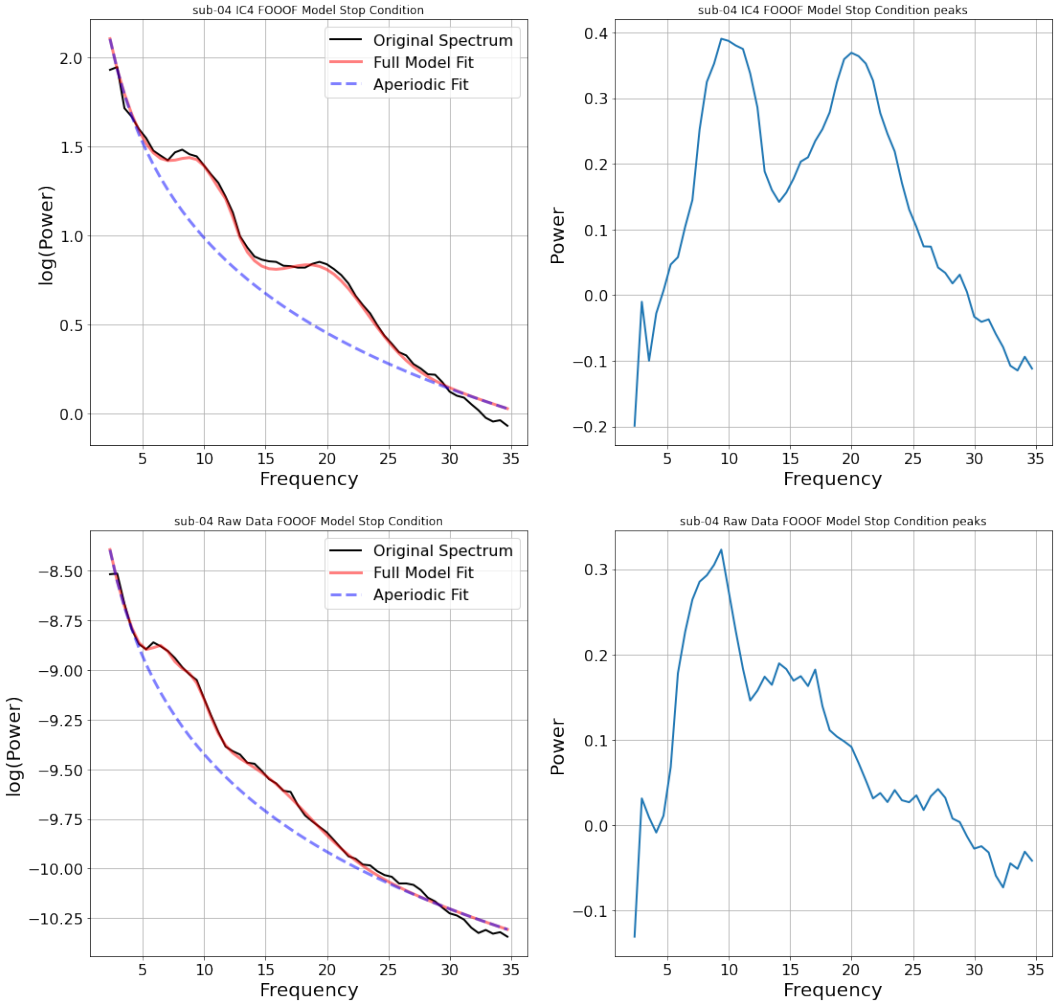

Figure 8: FOOOF analysis between the data after the subject IC was chosen (top row) and the raw data pre-ICA (bottom row).

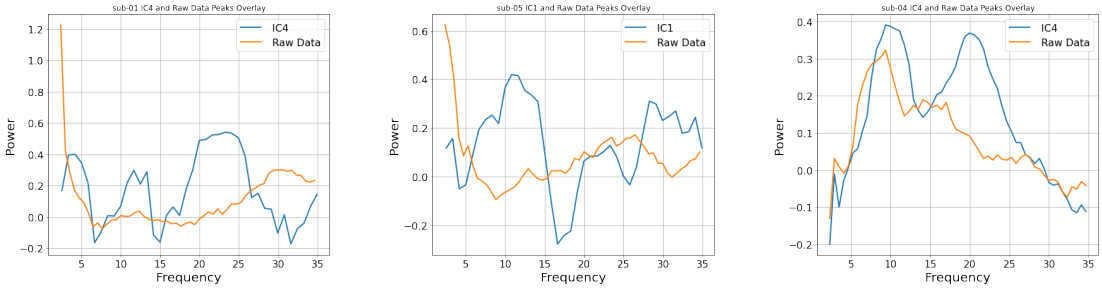

Figure 9: FOOOF peaks between the raw data pre-ICA (orange) and the subject IC (blue), after the removal of the aperiodic component.

5.6 Common Spatial Patterns

The CSP algorithm was used on each subject's session recordings and output a set of spatial patterns for a) pre-defined frequency band, and b) subject-specific frequency band determined from FOOOF. CSP would provide an estimator that transforms the input to maximizes the differences between two or more classes. Within the CSP pipeline, a frequency range could be provided to the filter bank to help with the discrimination between the classes.

The provided classes for the CSP algorithm were Go trials and Stop trials. In the CSP output, the first spatial pattern was the algorithm's weights for maximizing the variance for all Go trials and minimizing the variance for all Stop trials. The second spatial pattern was optimized in the inverse condition, maximizing the variance for all Stop trials and minimizing the variance for all Go trials. When paired, these spatial filters are a collection of features that help to discern one class from another. Overall, the resulting CSP modelling pipeline was a set of features for transforming incoming trials to map the signals into a latent space for more accurate classification. This process was evaluated for each subject in a machine learning pipeline, and the trials in the testing set were classified as either Go trials or Stop trials after being estimated by the CSP spatial filter. The LDA, SVM, and RF classifiers were discussed in the methods section; however, only the best performing classifier will be discussed further for comparing CSP guided with broad beta and subject beta activity.

Most subjects had more favourable neural topologies after using the subject-specific band, which includes characteristics such as increased weights on the electrodes near the centre of the scalp, decreased weights on areas close to muscle, or decreased resemblance to known topology patterns trained on noise or artifacts[138].

5.6.1 Model performance of classification algorithms compared between default beta and subject specific beta with CSP estimation

Various classifiers leverage the CSP estimator output differently, and it was important to compare the classification performance between these classifiers and whether using a subject-specific beta range could result in increased performance. The overall area under the curve in each ROC curve were recorded, but the shape of the curve and standard deviation error shading

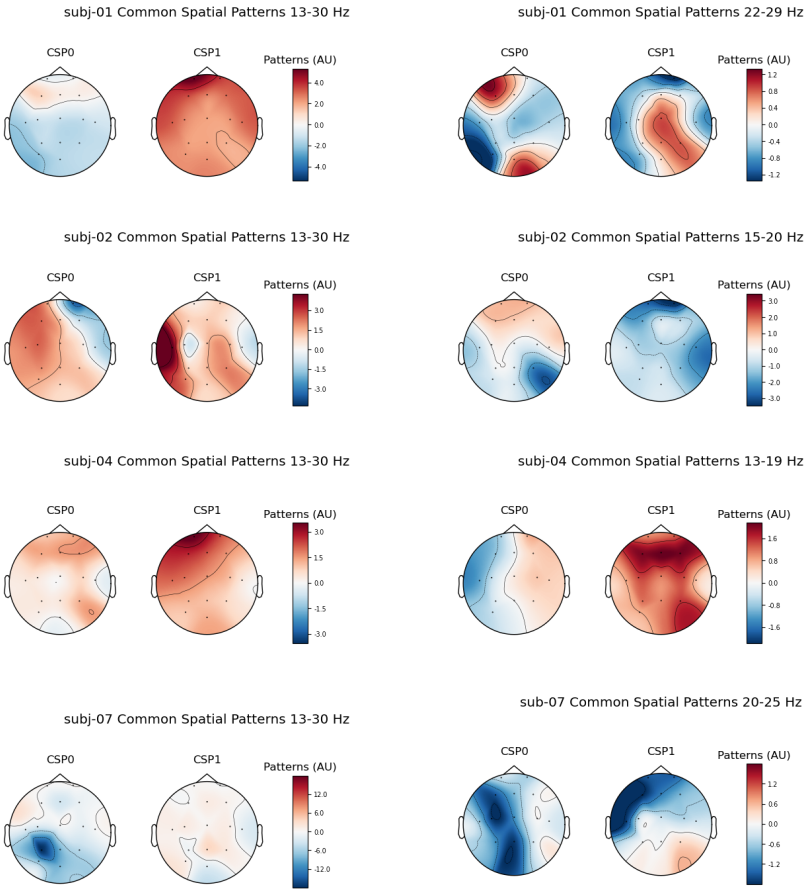

Figure 10: Comparison between using the full beta band and the subject specific beta for 4 selected subjects. The left column contains spatial patterns constructed with the default beta band, and the right column contains the respective subject-specific narrow bands.

were put into consideration.

The trials were transformed by the CSP estimator that was fitted on the labeled trials, and their patterns were visualized in Figure 10. This transformation step was first in the pipeline in the classification between go and stop trials. After normalization, the features were passed into the following classifiers and scored through cross validation (Figure 11 to Figure 13).

The ROC was evaluated over numerous iterations and folds. The shaded region was +/- 1 standard deviation from the curve. The average area under the curve (AUC) for between the broad beta activity range and subject beta ranges were similar for each model, but in the subject beta condition the curves appeared to lean toward the top left. In the random forest

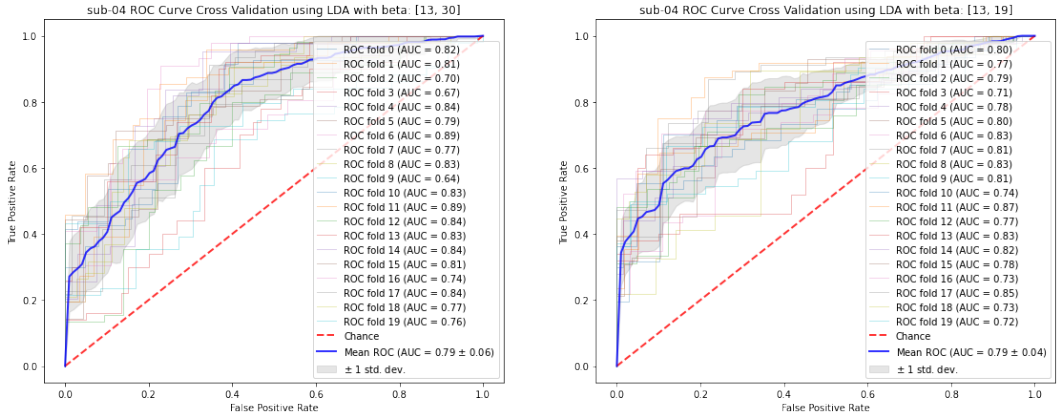

Figure 11: The LDA model performance trained on data with the CSP estimator in two conditions: CSP on default beta range and CSP on subject-specific beta ranges.

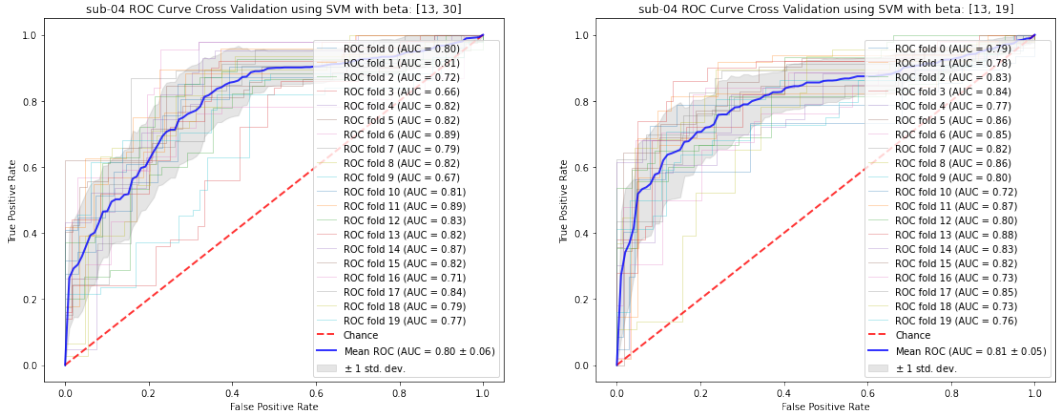

Figure 12: The SVM model performance trained on data with the CSP estimator in two conditions: CSP on default beta range and CSP on subject-specific beta ranges.

model, the AUC was higher than the same pipeline using LDA and SVM for all subjects. In the following analysis steps for confusion matrices and sliding windows, only the random forest model performance metrics will be shown for discussion.

5.6.2 Confusion matrix comparison between broad and subject-specific beta activity with random forest classification

Confusion matrices were constructed to visualize the recall and precision performance of the classification pipeline, and to further visualize which metric the subject-specific beta improved. A perfect confusion matrix would be a clear line from the top left to the bottom right. Between

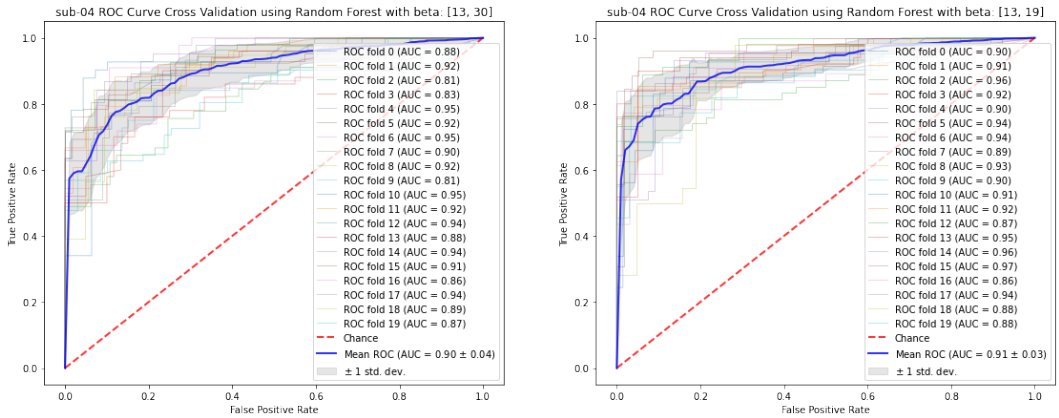

Figure 13: The RF model performance trained on data with the CSP estimator in two conditions: CSP on default beta range and CSP on subject-specific beta ranges.

the broad and subject-specific conditions, comparing how light the bottom left quadrant was would address misclassified stops, and comparing how much darker the bottom right quadrant was would address how much more a condition correctly captured Stop trials.

For every subject, the recall for the stop condition improved when using the subject-specific beta, shown qualitatively in the confusion matrices (Figure 14 and quantitatively in Table 2). There were almost no misclassified Go trials, shown by the nearly white top right quadrant and very dark top left quadrant.

5.6.3 Random forest classification over time

The RF model showed excellent performance in cross validation for classifying trial types. This performance was visualized throughout the time course of the trial by using a sliding window and scoring the model's prediction (Figure 15). The stop trial condition was not distinguishable until the stop stimulus occurred, and was represented by both chance level model performance until approximately 150 ms after the imperative (Figure 15a) and dense shading in the corresponding ERSP (Figure 15c).

5.6.4 Spatial and multilabel saccade classification performance with recorded data

In this section, the same analytical workflow with the CSP estimator and classification was used, except the classes were saccade-related. Within each epoch, the time-locked feature was

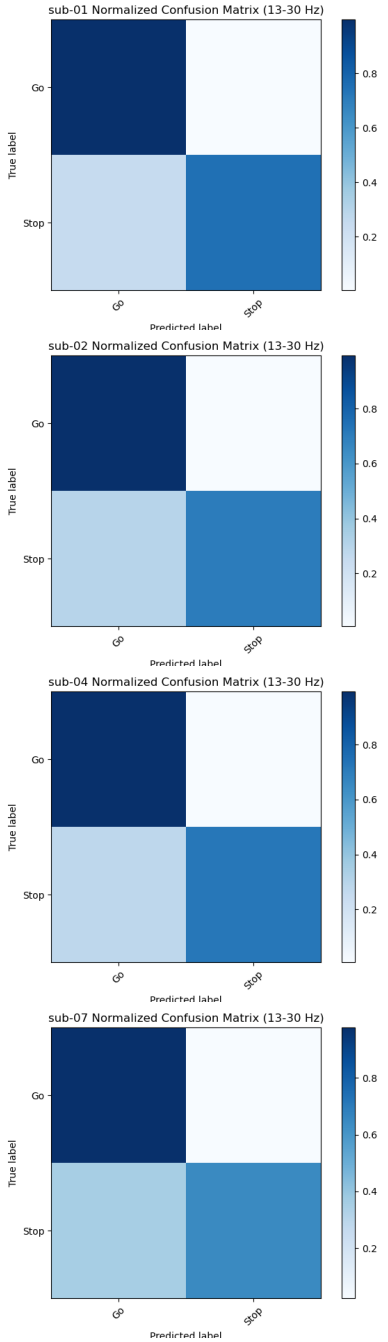

(a) Confusion Matrices with broad beta

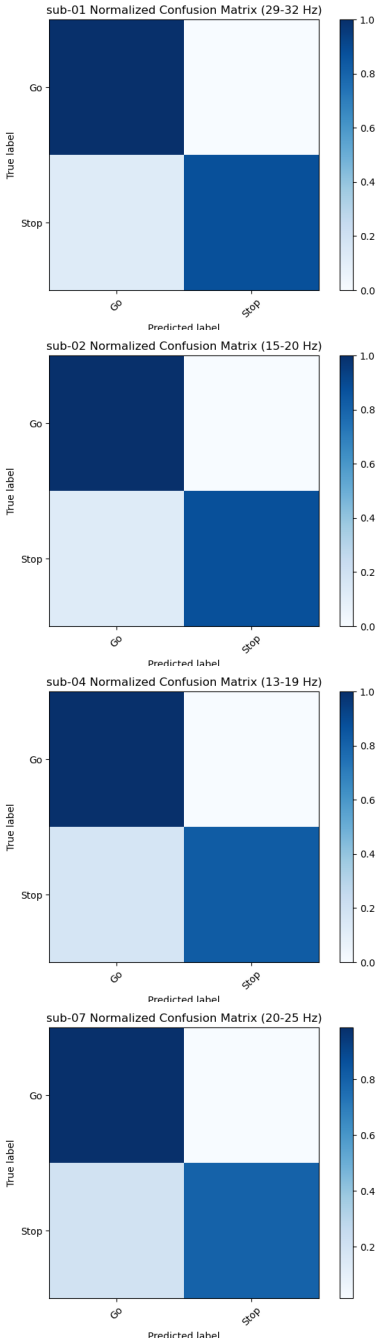

(b) Confusion matrices with subject beta

Figure 14: The confusion matrices for some selected subjects when comparing classification performance using broad beta (left column) and subject specific beta (right column). Each one was normalized so that each cell could be represented on a scale from 0 to 1.

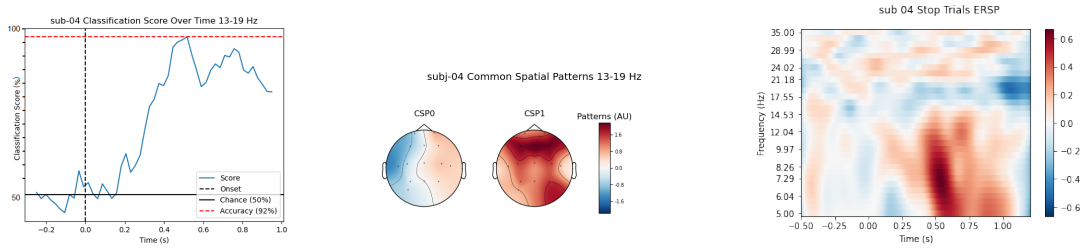

(a) Sliding window scoring (b) CSP estimator patterns (c) ERSP time frequency

Figure 15: Classification over time of a trial for a subject and the ERSP. (a) The black horizontal line at the bottom was the chance level drawn at 50% and the red dotted horizontal line at the top represented the overall trial accuracy. Although the pipeline was trained per trial, this graph showed the model performance over time by scoring iteratively through a sliding window. (b) The associated CSP topology for a given subject, representing the model weights from the CSP estimator to help classify whether the current signals are Go or Stop. (c) The ERSP throughout the trial, where 0.00s represented the time the fixation point disappeared. The activity of the ERSP temporally correlates with the likelihood of a successful classification as the trial progresses in a.

Subject	Broad Beta Stop Recall	Broad Beta F1 Score	Subj. Beta Stop Recall	Subj. Beta F1 Score	Stop Recall Change	F1 Score Change
01	0.7436	0.8924	0.8817	0.9483	13.81%	5.59%
02	0.7405	0.8887	0.8757	0.9445	13.52%	5.58%
03	0.7981	0.9166	0.8431	0.9312	4.51%	1.46%
04	0.7321	0.8817	0.8354	0.9279	10.33%	4.61%
05	0.6667	0.8590	0.7111	0.8793	4.44%	2.03%
06	0.6647	0.8554	0.7949	0.9111	13.02%	5.58%
07	0.6585	0.8464	0.7905	0.8987	13.20%	5.24%

Table 2: Classification scores summary across all subjects between CSP estimated using broad beta and their respective subject specific beta ranges.

the target presentation, and a trial's main differentiators were the instruction (saccade type) and spatial stimulus (direction). Saccade types were prosaccade or antisaccade, and saccade direction were left or right. In Figure 16, only the epochs containing a saccade were used (go trials) to differentiate between direction and instruction features.

The confusion matrix had a reasonable F1 score of 0.78 and discernible diagonal (Figure 16a), with the majority of misclassifications from wrongly predicting a right antisaccade as a left prosaccade on the bottom left. The antisaccade trials were rarely misclassified as prosaccade trials, depicted from the lack of shading on the top right. The CSP spatial filters from the estimators prior to classification were visualized (Figure 16b) and had greater spatial weights in

the frontal regions.

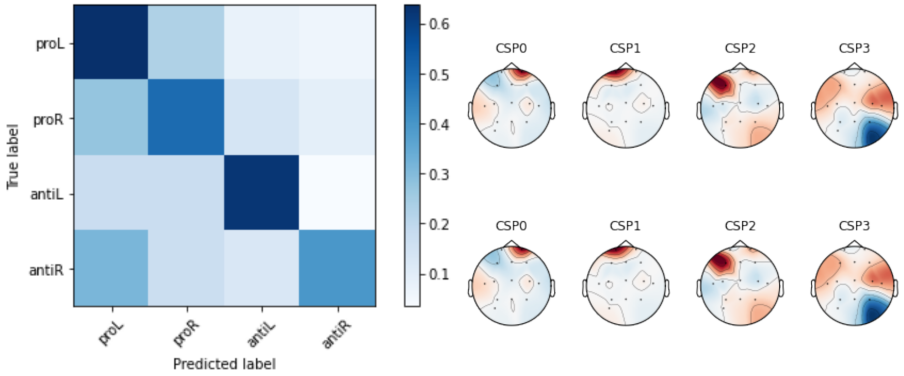

(a) Saccade cue and direction decoding. (b) CSP estimation step spatial patterns.

Figure 16: (a) Normalized confusion matrix showing model performance when scored on a naive subject recording session. The initial model was trained from a session recorded previously from the same subject. The model performance was depicted here through the shading. Increased performance was when a trial's predicted label aligned with the true label. The F1-score was 0.78. (b) CSP algorithm spatial filters displayed here during the estimator step of the classification pipeline.

6 Chapter 6: Discussion

6.1 Key signature changes identified in the EEG profile during the imperative phase

Two major ERP components have been investigated in Go/Stop tasks for the past 30 years: the N2 and P3 waveforms from the imperative cue. The N2 component describes a negative potential within a latency of 200-300 ms that is generated during Stop trials and reflects an inhibitory neuronal process from the BG-thalamocortical loop [43]. The P3 component follows at a latency of 300-600 ms after the imperative cue, and describes a peak that is also modulated in Stop conditions [43]. In our proposed task, the N2/P3 complex in the ERP was present in all subjects during the successful completion of a countermand (revoking a planned action) stop trial (Figure 5). In comparison across subjects, the latency of the N2/P3 complex onset was expected to differ because the stop signal delay was scaled towards the subject's performance. Time locking the trials to the onset of the stop signal delay would align the N2/P3 complex for all subjects, but this study's objective was to find subject specific neural correlates to generalize within subject states, rather than generalizing across subjects. Subject states are important to profile in brain-computer interfaces and closed-loop clinical systems to uphold reliable classification - well-timed and correct feedback to subjects reinforces the utility of neurofeedback. The same standard must be held here: the proposed subject-specific profile should detect states of free movement and states of rigidity or response inhibition. Maintaining temporal precision when differentiating between the movement and stop conditions would be essential for the subject's model to learn the appropriate features when training. For example, a saccade detection model would combine a spatial filter for saccade type (prosaccade, antisaccade) and a spatial filter for direction (left, right) in the classification and decoding of multi-labeled trials. It was imperative that each filter learned features relevant to their classification condition, such that the prominent spatial topologies and temporal sliding window classification (Figure 15a) were instrumental estimators after model training.

6.1.1 Event related spectral perturbation suggested frequency characteristics in stop trials

The ERSP for every subject suggested a large involvement of oscillatory characteristics in the alpha and beta range throughout the imperative epoch (Figure 6). Visualizing the ERSP in the preliminary steps was essential for confirming that the behavioural task was capable of evoking the neural processes involved in response inhibition in a trial-by-trial manner. This was qualitatively portrayed by the large red gradients that occurred 500 ms after the imperative, and a relative absence of activity along the baseline prior to the stimulus. The red gradients suggested phase synchronization, and the blue suggested phase de-synchronization in the frequency ranges encompassed by the shading. These ERP and ERSP patterns are similar to those reported in previous studies of countermanding [43,85,139].

Although there were qualitative similarities in the ERP's and ERSP's, the specific temporal and frequency patterns appeared unique in every subject. For example, some subjects had a larger distinction between their alpha and beta ranges, and some subjects showed later activation of phase synchrony. Although these aspects could likely be corrected to show the effect of the task condition across all subjects, the objective and scope of this paper was to extract features to model within subject states. Exploring correlates within subject states would enhance sensitivity for differentiating between cognitive states such as the response inhibition state (stop) and the movement state (go). The distinct features detailed above in the ERSP were qualitative, but suggested that quantitative analyses in the frequency domain (ICA) and time domain (CSP) could be potential methods for modelling these neural characteristics.

6.2 ICA contained task-modulating component in all healthy subjects

Since tasks involving response inhibition serve to probe the subject's ability to revoke a planned action, it does not matter whether the task was completed using hand movements or saccades. ICA separates mixed signals into their source components, and its use cases for separating movement artifacts from cognitive sources were documented extensively [105,118,140]. Our ERP isolated from ICA resembled the ERP from Wessel et al., 2019 [80], exhibiting increased weights on the sensorimotor region (Figure 7). This provides further validation of the novel

saccade task, and that the suppression of a pre-planned saccade utilizes an analogous pathway to one involved in the suppression of a pre-planned somantic motor command.

The spectrogram from this task-relevant component suggests some degree of phase synchrony in the beta band, such as the narrow region between 15-20 Hz in sub-04. Frequency characteristics were expected to be shown in components isolated using ICA, because ICA primarily operates on the frequency domain. This unique narrow band beta was detected in every subject, and could be better visualized and quantified with the FOOOF modelling approach.

6.3 FOOOF analysis shows unique subject-specific narrow beta peaks

FOOOF provides a systematic way to identify differences in power spectra across subjects. After the subtraction of the aperiodic component, the model oscillatory peaks are indicative of phase coupling within the frequency ranges of the peak (bandwidth) during the duration of the stop trial. Since the epochs were successful stop trials, the extracted peaks indicate that this narrow beta frequency band increase in power during the successful completion of a stop trial at the source location defined by the IC scalp topography. This was expected as increased synchrony of beta oscillations has been shown in motor inhibition[10,15,111], and stop signal tasks[37,81]. FOOOF can determine specific frequency ranges of subject beta measured in centre frequency, bandwidth, and power, and may be beneficial for finding characteristics of beta correlated to the prevalence and onset of Parkinson's disease.

6.3.1 FOOOF shows otherwise undetected features lost during traditional Fourier methods

Previous work has shown that traditional Fourier filtering methods destroy and potentially alter both phase-dependent and phase-independent waveform features of beta activity[12,19], such as higher frequency oscillations that can modulate beta-range activity[112]. When the FOOOF model was fitted on a task modulating IC, the model was able to detect narrow peaks in the beta range that were not present in the FOOOF model of the original data (Figure 8, Figure 9). Thus, some of the favourable features of ICA become evident after applying FOOOF. ICA is unsupervised and reveals latent spaces that are decorrelated from one another. In many cases,

this enhances the detectability of signals, and ICA can also be used to remove unwanted biological artifacts[105]. The peaks were evaluated following the neurophysiological signatures of response inhibition shown previously using ICA, and the range of the extracted peaks were systematically determined on all subjects (Table 1).

6.3.2 Two spectral components involved in freezing of gait

Oscillations in the narrow band beta range (18 Hz) have been characterized to correlate with the vulnerability to FOG in PD patients[62]. Chen et al had also found that two spectral activities in the STN region (5-8 Hz, and 15-21 Hz) were associated with FOG. Our findings show that the stop condition in our stop signal task was able to invoke these two significant spectral ranges in the periodic component of alpha and beta in nearly all subjects (Table 1). Although our test subjects were healthy volunteers, this task was designed to reflect BG activity through response inhibition. The action selection during the stop condition activates the same neural circuitry as unexpected stopping despite having top-down involvement[85,88,141]. These results strengthen the literature associated with the traditional hand-motor stop signal task and our novel saccade-based counterpart. Furthermore, FOOOF provides a potential PD neural correlate when fitted on the component that modulates during the stop condition. This dual spectral neural correlate may potentially reflect both unexpected stopping and FOG timed with pathological oscillations from the STN. Further research on STN signals from PD patients with DBS would be necessary to definitely determine this link.

6.4 Common Spatial Patterns use subject-specific parameters to construct task modulating spatial patterns

The initial fit of the CSP model with the subject-specific beta range extracted from ICA-FOOOF showed topographies that resemble neural patterns (Figure 10). It was important to confirm that CSP did not favour spatial characteristics resembling artifacts such as muscle, eye-movements, and ECG, because these artefact features tend to be more detectable on the scalp than neural signals from the brain. The narrow subject-specific band was expected to have minimal presence of these artifacts and expected to enhance the detection of relevant beta

activity via increased SNR. Despite the known literature of frequency ranges of these artefacts and modern preprocessing techniques for their removal, the spectral bandwidth of muscle activity remains vast at between 20 Hz to 300 Hz[138].

CSP had been successful in assistive brain computer interfaces for spellers[120], as the modeling approach would construct as many spatial filters needed (ie: for each letter during spelling) and classification was optimized accordingly through various hyperparameters. However, in the early stages of training, the correct identification of neural features is more crucial than modelling accuracy. Unlike the manual selection and justification from the ICA pipeline, this preliminary approach with CSP attempts to avoid biases (ERP complexes) with the exception of ensuring the constructed spatial patterns to be of neural characteristics, as discussed above (Figure 10). Since the ERP complexes were confirmed to be present in the ICA analysis without introducing experimenter bias, the classification pipeline should not be overfitted to this simple feature that was readily detectable.

6.4.1 Increased classification performance between Go and Stop conditions using subject specific beta

The receiver operating characteristic (ROC) curve graphed for each constructed classifier is a common metric for evaluating the performance of classification in machine learning[142]. A perfect classifier would have the characteristic of the drawn curve straight up to the top left and then traversed all the way to the top right, or an AUC of 1. A classifier with an AUC of 0.50 or sometimes even lower would indicate how it performs compared to chance, visualized by the diagonal $y = x$ line

Heavily biasing the model to increase classification performance would lead to overfitting and failure for the model to perform adequately in data outside of its training set. In practical applications, reducing the bias and regulating the variance to low but not non-negligible levels are all imperative[143]. The choice to introduce a subject-specific beta parameter for optimizing the model was primarily to ensure that the model would train on relevant neural activity rather than noise or artifacts, as the same-session model performance changes were likely not significant. A series of classifiers were tested to see how various models could leverage the CSP estimator on broad or subject-specific beta (Figure 11, Figure 12, Figure 13). Nearly all scenarios for cross

validation showed increased classification performance when using the subject-specific beta, with the random forest classifier performing the best in both AUC and shape of the ROC curve (Figure 13). Furthermore, during inference on a separate session the subject-specific model performed better without re-training: suggesting that the trained features generalized well and were not overfitted to session specific noise (Figure 14).

6.4.2 Random forest showed increased classification performance when CSP estimator used subject beta

There was some misclassification during the proper prediction of go trials, depicted by the bottom left square of the confusion matrices in Figure 14a. This would be the false negative rate if Go was the negative prediction and Stop was the positive prediction for effect in this binary classification. After using subject-specific ranges on the identical pipeline, the bottom left squares appeared lighter qualitatively (Figure 14b), and quantitatively the stop recall value increased for all subjects (Table 2). In addition, the box on the bottom right depicting the true positive rate (successful classification of stop trials) also appeared darker, and these performance gains were portrayed by an increase in the overall F1 score.

A possible explanation for increased recall for the stop condition was that the narrow subject beta frequencies were more characteristic of stop trials. This was supported by the darker bottom right square mentioned previously, as well as the white square on the top right. This white square (false positive rate), indicating the absence of wrongly predicting a stop trial, occurred in all cases; the broad beta was not able to capture all the true stop trials, but it did not misclassify them. The correct classification of Go trials was very high in both the broad and narrow band CSP estimators, which may imply that frequency characteristics of the go trial may be present or entangled in both conditions.

6.4.3 Random forest algorithm shows task predictive features on the time domain

Although CSP is a supervised algorithm for differentiating between labeled classes, the model's accuracy throughout the trial (sliding window) should resemble that of the subject's intuition, and trained appropriately as CSP is sensitive to space and time. This means that during the evaluation of new neural data, the model cannot make a decision before the sub-

ject processes the stop signal. The Go condition contained a saccade that occurred on average 300-500 ms from the time-locked imperative. The Stop condition stimulus occurred on average 150-200 ms after the time-locked imperative, and the highly classified neural signatures of stopping (N2/P3 complex) would occur 300 ms after the stop stimulus (or 500 ms from the time-locked imperative). This would suggest that a successful classifier would perform by chance for approximately the first 200 ms of the epoch, and be capable of differentiating between the two classes afterwards. This was observed in the classification accuracy throughout the duration of the epoch for each subject (Figure 15), with chance probabilities prior to the stop stimulus (approximately 200 ms), and reaching maximum at approximately 500 ms. This correctly aligned with the subject's intuition, that the model had no way of determining whether the task was a stop signal until at least 200 ms after the imperative.

6.4.4 Classifying antisaccade biomarkers of disease

Abnormalities in performing antisaccade tasks have been linked to PD disease phenotypes, such as abnormalities in saccade characteristics (saccade error[29,31,32], velocity[33]), and gait[59,60], electrophysiological increases in beta synchrony[41], and disease progression[60]. To provide maximum flexibility for future PD experiments, we developed a workflow to differentiate between saccade types trained on each subject. Our machine learning pipeline determines the optimal transformations necessary to localize sources of interest during saccade tasks optimized systematically without bias (ie: classification, independence or likelihood, etc.). This yielded spatial filters that could decode the saccade types (prosaccade, antisaccade) and direction (left, right) at a high level of confidence (Figure 16). For successful multi-label classification, recordings must be captured with spatial and temporal precision as direction and instruction features could overlap. For example, epochs containing left saccades could be either prosaccade or antisaccade, and vice versa for right saccades. This was a proof of concept that the experimental platform could capture spatiotemporal features with high fidelity despite this overlap of features, and that a machine learning model could learn to disentangle more than one feature in an epoch.

This is a novel finding as prior saccade literature in electrophysiology typically focuses on classifying saccades by latency differences and saccade characteristics (velocity, vigor), whereas the work denoted here used purely electrophysiology data. In future PD patients, machine

learning spatial filters can be decomposed for researchers to learn or confirm metrics, since each model can be visualized as feature importance - where features and parameters are quantified to the degree they influence the model (ie: features such as, source location, oscillatory power, and reaction time can be quantified in percentages per trial to show their importance in the model's final decision).

In summary, verifying the hallmarks of inhibitory control was necessary in our novel saccade task delivered in VR in order to address our hypothesis that BG activation for controlling saccades utilizes a parallel pathway as the one involved in hand motor movements. Similar to the N2/P3 complex, ERSP latencies were within expected ranges, and the sources isolated from ICA resembled response inhibition characteristics found in previous hand-motor studies[79,80]. The experimental platform was newly developed to facilitate future saccade-based combined psychophysical-electrophysiological studies (supplementary material in the appendix). The results from these subjects portray a successful early implementation of this platform. Our ERP results indicated proper alignment of all trials during averaging of the electrical activity, and our analysis pipeline details more advanced analysis tools for elucidating the neural processes involved in the task conditions, than previously used.

The time-frequency analysis clearly demonstrated that each subject showed unique oscillatory characteristics throughout the time window of the trials. Spatial, frequency, and temporal features are a) necessary for subject-specific modeling, b) reliably recorded by our labstreaming layer based experimental platform, and c) preserved throughout the analysis pipeline. In the illustrated pipeline, ICA isolates source signals that modulate with the task condition, and FOOOF determines the oscillatory characteristics that contribute to these source signals in the subject-specific frequency domain. The classification pipeline leverages this subject-specific domain to construct spatial-temporal filters that could predict the trial conditions in both trial-by-trial classification (Figure 14b, Figure 15b) and within trial classification (Figure 15a). In this controlled setting, the classifier could reliably predict the onset of the recruitment of neural processes related to response inhibition (Table 2). In future real-time applications, this model could continuously process the current state of the patient, similar to the sliding window classification in Figure 15a, and alert the patient when electrical signals related to stopping are detected (crossing the threshold of predicting normal movement versus rigidity).

7 Conclusion

The experimental platform was capable of reliably capturing neural and behavioural data while displaying a task in VR controlled by eye movements. The proposed stop signal task using saccades was shown to evoke beta modulation in the Stop condition in healthy subjects. Methodologies for extracting subject-specific frequency ranges were successful, and preliminary modelling with machine learning of each subject's neural data between the Stop condition and Go conditions was done.

This thesis outlined the rationale and methodology behind the development of a clinical neurophysiology psychophysics framework and presented the preprocessing procedures for transforming unstructured data into formats ready for machine learning pipelines. The full lifecycle of the machine learning pipeline was documented and utilized for real-time inferencing. This project is REB approved for conducting behavioural experiments at the OHRI and continues to be in active development.

7.1 Future Considerations

The experimental platform and processing pipeline were developed with the intention of applying to future experiments on patients with Parkinson's disease to better understand the mechanisms of disease and the neurophysiological correlates. Possible experiments could include repeating the current tasks with participants on and off levodopa, during DBS surgery with microelectrode recordings within the STN, and/or after surgery with the DBS turned off versus on. The model pipeline will contain parameters optimized for each patient, and can automatically learn to hyperparameterize features related to disease progression for use in DBS surgery during target localization.

In addition, the established pipeline for data acquisition to model preprocessing allows flexibility in choosing various modelling algorithms and classifiers. For example, replacing the Random Forest classifier with another modelling technique, or adding a regression estimator like source power comodulation (SPoC). As DBS devices devices continue to evolve, with DBS implants allowing for wireless communication and closed-loop implementation, the demand for platforms needed to explore electrophysiological biomarkers will continue to grow.

References

[1] Jose A. Obeso, Maria Cruz Rodríguez-Oroz, Beatriz Benitez-Temino, Francisco J. Blesa, Jorge Guridi, Concepció Marin, and Manuel Rodriguez. Functional organization of the basal ganglia: Therapeutic implications for Parkinson's disease. *Movement Disorders*, 23 (SUPPL. 3):548–559, 2008. ISSN 08853185. doi: 10.1002/mds.22062.

[2] Masayuki Watanabe and Douglas P. Munoz. Probing basal ganglia functions by saccade eye movements. *The European journal of neuroscience*, 33(11):2070–90, 6 2011. ISSN 1460-9568. doi: 10.1111/j.1460-9568.2011.07691.x. URL `http://doi.wiley.com/10.1111/j.1460-9568.2011.07691.x` `http://www.ncbi.nlm.nih.gov/pubmed/21645102`.

[3] Alexander Blenkinsop, Sean Anderson, and Kevin Gurney. Frequency and function in the basal ganglia: the origins of beta and gamma band activity. *The Journal of Physiology*, 595(13):4525–4548, 7 2017. ISSN 00223751. doi: 10.1113/JP273760.

[4] Alia Tewari, Rachna Jog, and Mandar S. Jog. The Striatum and Subthalamic Nucleus as Independent and Collaborative Structures in Motor Control. *Frontiers in Systems Neuroscience*, 10(March):1–13, 2016. ISSN 1662-5137. doi: 10.3389/fnsys.2016.00017. URL `http://journal.frontiersin.org/article/10.3389/fnsys.2016.00017`.

[5] Harvey S Singer, Jonathan W Mink, Donald L Gilbert, and Joseph Jankovic. Chapter 1 - Basal Ganglia Anatomy, Biochemistry, and Physiology. page 7.

[6] José L Lanciego, Natasha Luquin, and José A Obeso. Functional neuroanatomy of the basal ganglia. *Cold Spring Harbor perspectives in medicine*, 2(12):a009621, 12 2012. doi: 10.1101/cshperspect.a009621. URL `http://dx.doi.org/10.1101/cshperspect.a009621`.

[7] C J Wilson. Striatum: Internal Physiology. In *Encyclopedia of Neuroscience*, pages 563–572. Elsevier, 2009. ISBN 978-0-08-045046-9.

[8] Hagai Bergman, Thomas Wichmann, and M. DeLong. Reversal of experimental parkinsonism by lesions of the subthalamic nu-

cleus. *Science*, 249(4975):1436–1438, 9 1990. ISSN 0036-8075. doi: 10.1126/science.2402638. URL http://dx.doi.org/10.1126/science.2402638 https://www.sciencemag.org/lookup/doi/10.1126/science.2402638.

[9] A Berardelli, J C Rothwell, P D Thompson, and M Hallett. Pathophysiology of bradykinesia in Parkinson's disease. *Brain: A Journal of Neurology*, 124(Pt 11): 2131–2146, 11 2001. ISSN 0006-8950. doi: 10.1093/brain/124.11.2131. URL http://dx.doi.org/10.1093/brain/124.11.2131.

[10] Alejo J. Nevado Holgado, John R. Terry, Rafal Bogacz, Alejo J Nevado Holgado, John R. Terry, and Rafal Bogacz. Conditions for the generation of beta oscillations in the subthalamic nucleus-globus pallidus network. *The Journal of Neuroscience*, 30(37): 12340–12352, 9 2010. ISSN 02706474. doi: 10.1523/{JNEUROSCI}.0817-10.2010. URL http://dx.doi.org/10.1523/https://www.jneurosci.org/content/30/37/12340 https://www.jneurosci.org/content/30/37/12340.abstract.

[11] Elizabeth Heinrichs-Graham, Max J. Kurz, Katherine M. Becker, Pamela M. Santamaria, Howard E. Gendelman, and Tony W. Wilson. Hypersynchrony despite pathologically reduced beta oscillations in patients with Parkinson's disease: a pharmaco-magnetoencephalography study. *Journal of Neurophysiology*, 112(7): 1739–1747, 10 2014. ISSN 0022-3077. doi: 10.1152/jn.00383.2014. URL https://www.physiology.org/doi/10.1152/jn.00383.2014.

[12] Nicko Jackson, Scott C Cole, Bradley Voytek, and Nicole C Swann. Characteristics of Beta Waveform Shape in Parkinson's Disease Detected with Scalp Electroencephalography. *BioRxiv*, 1 2019. doi: 10.1101/534396. URL http://biorxiv.org/lookup/doi/10.1101/534396.

[13] Coralie de Hemptinne, Nicole C Swann, Jill L Ostrem, Elena S Ryapolova-Webb, Marta San Luciano, Nicholas B Galifianakis, and Philip A Starr. Therapeutic deep brain stimulation reduces cortical phase-amplitude coupling in Parkinson's disease. *Nature Neuroscience*, 18(5):779–786, 5 2015. doi: 10.1038/nn.3997. URL http://dx.doi.org/10.1038/nn.3997.

[14] Gerd Tinkhauser, Alek Pogosyan, Simon Little, Martijn Beudel, Damian M. Herz, Huiling Tan, and Peter Brown. The modulatory effect of adaptive deep brain stimulation on beta bursts in Parkinson's disease. *Brain*, 140(4):1053–1067, 4 2017. ISSN 0006-8950. doi: 10.1093/brain/awx010.

[15] Simon Little and Peter Brown. The functional role of beta oscillations in Parkinson's disease. *Parkinsonism & Related Disorders*, 20 Suppl 1(SUPPL.1): S44–S48, 1 2014. ISSN 13538020. doi: 10.1016/S1353-8020(13)70013-0. URL http://dx.doi.org/10.1016/S1353-8020(13)70013-0.

[16] M. M. McCarthy, C. Moore-Kochlacs, X. Gu, E. S. Boyden, X. Han, and N. Kopell. Striatal origin of the pathologic beta oscillations in Parkinson's disease. *Proceedings of the National Academy of Sciences*, 108(28):11620–11625, 7 2011. ISSN 0027-8424. doi: 10.1073/pnas.1107748108. URL http://dx.doi.org/10.1073/pnas.1107748108 http://www.pnas.org/cgi/doi/10.1073/pnas.1107748108.

[17] Preeya Khanna, Nicole C. Swann, Coralie de Hemptinne, Svjetlana Miocinovic, Andrew Miller, Philip A. Starr, and Jose M. Carmena. Neurofeedback Control in Parkinsonian Patients Using Electrocorticography Signals Accessed Wirelessly With a Chronic, Fully Implanted Device. *IEEE Transactions on Neural Systems and Rehabilitation Engineering*, 25(10):1715–1724, 10 2017. ISSN 1534-4320. doi: 10.1109/TNSRE.2016.2597243. URL http://dx.doi.org/10.1109/https://ieeexplore.ieee.org/document/7549053/.

[18] Ingrid H.C.H.M. C H M Philippens, Jacqueline A. Wubben, Raymond A.P. P Vanwersch, Dave L. Estevao, and Peter A. Tass. Sensorimotor rhythm neurofeedback as adjunct therapy for Parkinson's disease. *Annals of Clinical and Translational Neurology*, 4(8):585–590, 7 2017. ISSN 23289503. doi: 10.1002/acn3.434. URL http://dx.doi.org/10.1002/acn3.434.

[19] Scott R Cole and Bradley Voytek. Brain oscillations and the importance of waveform shape. *Trends in Cognitive Sciences*, 21(2):137–149, 1 2017. doi: 10.1016/j.tics.2016.12.008. URL http://dx.doi.org/10.1016/j.tics.2016.12.008.

[20] Oliver Bichsel, Lennart H Stieglitz, Markus F Oertel, Christian R Baumann, Roger Gassert, and Lukas L Imbach. Deep brain electrical neurofeedback allows Parkinson patients to control pathological oscillations and quicken movements. *medRxiv*, page 2020.06.10.20127829, 6 2020. doi: 10.1101/2020.06.10.20127829. URL https://doi.org/10.1101/2020.06.10.20127829.

[21] A. Gulberti, C. K.E. Moll, W. Hamel, C. Buhmann, J. A. Koeppen, K. Boelmans, S. Zittel, C. Gerloff, M. Westphal, T. R. Schneider, and A. K. Engel. Predictive timing functions of cortical beta oscillations are impaired in Parkinson's disease and influenced by L-DOPA and deep brain stimulation of the subthalamic nucleus Impaired beta-band timing functions in PD. *NeuroImage: Clinical*, 9:436–449, 2015. ISSN 22131582. doi: 10.1016/j.nicl.2015.09.013. URL http://dx.doi.org/10.1016/j.nicl.2015.09.013.

[22] L M F Doyle, A A Kühn, M Hariz, A Kupsch, G-H Schneider, and P Brown. Levodopa-induced modulation of subthalamic beta oscillations during self-paced movements in patients with Parkinson's disease. *The European Journal of Neuroscience*, 21(5):1403–1412, 3 2005. doi: 10.1111/j.1460-9568.2005.03969.x. URL http://dx.doi.org/10.1111/j.1460-9568.2005.03969.x.

[23] G Pfurtscheller. Functional brain imaging based on {ERD}/{ERS}. *Vision Research*, 41(10-11):1257–1260, 2001. doi: 10.1016/s0042-6989(00)00235-2. URL http://dx.doi.org/10.1016/s0042-6989(00)00235-2.

[24] Yvonne M Fonken, Jochem W Rieger, Elinor Tzvi, Nathan E Crone, Edward Chang, Josef Parvizi, Robert T Knight, and Ulrike M Krämer. Frontal and motor cortex contributions to response inhibition: evidence from electrocorticography. *Journal of Neurophysiology*, 115(4):2224–2236, 4 2016. doi: 10.1152/jn.00708.2015. URL http://dx.doi.org/10.1152/jn.00708.2015.

[25] Andreas K Engel and Pascal Fries. Beta-band oscillations–signalling the status quo? *Current Opinion in Neurobiology*, 20(2):156–165, 4 2010. ISSN 1873-6882. doi: 10.1016/j.conb.2010.02.015. URL http://dx.doi.org/10.1016/j.conb.2010.02.015.

[26] Bernhard Spitzer and Saskia Haegens. Beyond the Status Quo: A Role for Beta Oscillations in Endogenous Content (Re)Activation. *eneuro*, 4(4):0170–17, 7 2017. ISSN 2373-2822. doi: 10.1523/ENEURO.0170-17.2017.

[27] Ned Jenkinson and Peter Brown. New insights into the relationship between dopamine, beta oscillations and motor function. *Trends in Neurosciences*, 34(12):611–618, 12 2011. doi: 10.1016/j.tins.2011.09.003. URL http://dx.doi.org/10.1016/j.tins.2011.09.003.

[28] Michael J Frank, Johan Samanta, Ahmed A Moustafa, and Scott J Sherman. Hold your horses: impulsivity, deep brain stimulation, and medication in parkinsonism. *Science*, 318(5854):1309–1312, 11 2007. ISSN 1095-9203. doi: 10.1126/science.1146157. URL http://dx.doi.org/10.1126/science.1146157.

[29] Elena Pretegiani and Lance M. Optican. Eye movements in Parkinson's disease and inherited parkinsonian syndromes. *Frontiers in Neurology*, 8(NOV): 1–7, 11 2017. ISSN 16642295. doi: 10.3389/fneur.2017.00592. URL http://dx.doi.org/10.3389/fneur.2017.00592.

[30] Anshul Srivastava, Ratna Sharma, Sanjay K Sood, Garima Shukla, Vinay Goyal, and Madhuri Behari. Saccadic eye movements in Parkinson's disease. *Indian journal of ophthalmology*, 62(5):538–544, 5 2014. doi: 10.4103/0301-4738.133482. URL http://dx.doi.org/10.4103/0301-4738.133482.

[31] Florence Chan, Irene T. Armstrong, Giovanna Pari, Richard J. Riopelle, and Douglas P. Munoz. Deficits in saccadic eye-movement control in Parkinson's disease. *Neuropsychologia*, 43(5):784–796, 2005. ISSN 00283932. doi: 10.1016/j.neuropsychologia.2004.06.026. URL http://dx.doi.org/10.1016/j.neuropsychologia.2004.06.026.

[32] Courtney C. Walton, Claire O'Callaghan, Julie M. Hall, Moran Gilat, Loren Mowszowski, Sharon L. Naismith, James R. Burrell, James M. Shine, Simon J G Lewis, Claire O'Callaghan, Julie M. Hall, Moran Gilat, Loren Mowszowski, Sharon L. Naismith, James R. Burrell, James M. Shine, and Simon J G Lewis. Antisaccade errors reveal cognitive control deficits in Parkinson's disease with freezing of gait. *Journal of Neurol-*

ogy, 262(12):2745–2754, 12 2015. ISSN 14321459. doi: 10.1007/s00415-015-7910-5. URL http://dx.doi.org/10.1007/s00415-015-7910-5.

[33] Ashley J Hood, Silvia C Amador, Ashley E Cain, Kevin A Briand, Ali H Al-Refai, Mya C Schiess, and Anne B Sereno. Levodopa slows prosaccades and improves antisaccades: an eye movement study in Parkinson's disease. *Journal of Neurology, Neurosurgery, and Psychiatry*, 78(6):565–570, 6 2007. doi: 10.1136/jnnp.2006.099754. URL http://dx.doi.org/10.1136/jnnp.2006.099754.

[34] M. A. Basso and M. A. Sommer. Exploring the role of the substantia nigra pars reticulata in eye movements. *Neuroscience*, 198:205–212, 12 2011. ISSN 03064522. doi: 10.1016/j.neuroscience.2011.08.026. URL http://dx.doi.org/10.1016/j.neuroscience.2011.08.026.

[35] O Hikosaka. Basal Ganglia and Oculomotor Control. In Larry R B T Encyclopedia of Neuroscience Squire, editor, *Encyclopedia of Neuroscience*, pages 53–61. Elsevier, Oxford, 2009. ISBN 978-0-08-045046-9. doi: 10.1016/B978-008045046-9.01088-3.

[36] S Gauggel, M Rieger, and T-A Feghoff. Inhibition of ongoing responses in patients with Parkinson's disease. *Journal of Neurology, Neurosurgery, and Psychiatry*, 75(4):539–544, 4 2004. doi: 10.1136/jnnp.2003.016469. URL http://dx.doi.org/10.1136/jnnp.2003.016469.

[37] Jobi S. George, Jon Strunk, Rachel Mak-McCully, Melissa Houser, Howard Poizner, and Adam R. Aron. Dopaminergic therapy in Parkinson's disease decreases cortical beta band coherence in the resting state and increases cortical beta band power during executive control. {*NeuroImage*}. *Clinical*, 3:261–270, 8 2013. ISSN 22131582. doi: 10.1016/j.nicl.2013.07.013. URL http://dx.doi.org/10.1016/j.nicl.2013.07.013.

[38] Ignacio Obeso, Leonora Wilkinson, Enrique Casabona, Maarten Speekenbrink, María Luisa Bringas, Mario Álvarez, Lázaro Álvarez, Nancy Pavón, María C Rodríguez-Oroz, Raúl Macías, Jose A Obeso, and Marjan Jahanshahi. The subthalamic nucleus and inhibitory control: impact of subthalamotomy in Parkinson's disease. *Brain: A Jour-*

nal of Neurology, 137(Pt 5):1470–1480, 5 2014. doi: 10.1093/brain/awu058. URL http://dx.doi.org/10.1093/brain/awu058.

[39] Wery P. M. van den Wildenberg, Geert J. M. van Boxtel, Maurits W. van der Molen, D. Andries Bosch, Johannes D. Speelman, and Cornelis H. M. Brunia. Stimulation of the Subthalamic Region Facilitates the Selection and Inhibition of Motor Responses in Parkinson's Disease. *Journal of Cognitive Neuroscience*, 18 (4):626–636, 2006. ISSN 0898-929X. doi: 10.1162/jocn.2006.18.4.626. URL http://www.mitpressjournals.org/doi/10.1162/jocn.2006.18.4.626.

[40] Ian G M Cameron, Brian C Coe, Masayuki Watanabe, Patrick W Stroman, and Douglas P Munoz. Role of the basal ganglia in switching a planned response. *The European Journal of Neuroscience*, 29(12):2413–2425, 6 2009. doi: 10.1111/j.1460-9568.2009.06776.x. URL http://dx.doi.org/10.1111/j.1460-9568.2009.06776.x.

[41] Akihiro Yugeta, William D Hutchison, Clement Hamani, Utpal Saha, Andres M Lozano, Mojgan Hodaie, Elena Moro, and Robert Chen. Modulation of Beta Oscillations in the Subthalamic Nucleus with Prosaccades and Antisaccades in Parkinson's Disease. *Journal of Neuroscience*, 33(16):6895–6904, 4 2013. ISSN 0270-6474. doi: 10.1523/JNEUROSCI.2564-12.2013.

[42] Lisa C Goelz, Fabian J David, John A Sweeney, David E Vaillancourt, Howard Poizner, Leonard Verhagen Metman, and Daniel M Corcos. The effects of unilateral versus bilateral subthalamic nucleus deep brain stimulation on prosaccades and antisaccades in Parkinson's disease. *Experimental Brain Research*, 235(2):615–626, 2017. doi: 10.1007/s00221-016-4830-2. URL http://dx.doi.org/10.1007/s00221-016-4830-2.

[43] Hirokazu Bokura, Shuhei Yamaguchi, and Shotai Kobayashi. Event-related potentials for response inhibition in Parkinson's disease. *Neuropsychologia*, 43(6):967–975, 2005. doi: 10.1016/j.neuropsychologia.2004.08.010. URL http://dx.doi.org/10.1016/j.neuropsychologia.2004.08.010.

[44] Dejan Georgiev, Georg Dirnberger, Leonora Wilkinson, Patricia Limousin, and Marjan Jahanshahi. In Parkinson's disease on a probabilistic Go/NoGo task deep brain stimu-

lation of the subthalamic nucleus only interferes with withholding of the most prepotent responses. *Experimental Brain Research*, 234(4):1133–1143, 4 2016. ISSN 14321106. doi: 10.1007/s00221-015-4531-2. URL http://dx.doi.org/10.1007/s00221-015-4531-2.

[45] Angela L Holmes, Patrick A Forcelli, Jacqueline T DesJardin, Ashley L Decker, Menna Teferra, Elizabeth A West, Ludise Malkova, and Karen Gale. Superior Colliculus Mediates Cervical Dystonia Evoked by Inhibition of the Substantia Nigra Pars Reticulata. *Journal of Neuroscience*, 32(38):13326–13332, 9 2012. ISSN 0270-6474. doi: 10.1523/JNEUROSCI.2295-12.2012. URL https://www.jneurosci.org/lookup/doi/10.1523/JNEUROSCI.2295-12.2012.

[46] M. Sato and O. Hikosaka. Role of primate substantia nigra pars reticulata in reward-oriented saccadic eye movement. *The Journal of Neuroscience*, 22(6):2363–2373, 2002.

[47] Marina Senek, Sten Magnus Aquilonius, Håkan Askmark, Filip Bergquist, Radu Constantinescu, Anders Ericsson, Sara Lycke, Alexander Medvedev, Mevludin Memedi, Fredrik Ohlsson, Jack Spira, Jerker Westin, and Dag Nyholm. Levodopa/carbidopa microtablets in Parkinson's disease: a study of pharmacokinetics and blinded motor assessment. *European Journal of Clinical Pharmacology*, 73(5):563–571, 5 2017. ISSN 14321041. doi: 10.1007/s00228-017-2196-4.

[48] Sten-Magnus Aquilonius and Dag Nyholm. Development of new levodopa treatment strategies in Parkinson's disease-from bedside to bench to bedside. *Upsala journal of medical sciences*, 122(2):71–77, 6 2017. doi: 10.1080/03009734.2017.1285374. URL http://dx.doi.org/10.1080/03009734.2017.1285374.

[49] Anthony E Lang and Jose A Obeso. Challenges in Parkinson's disease: restoration of the nigrostriatal dopamine system is not enough. *The Lancet Neurology*, 3(5):309–316, 2004. ISSN 1474-4422. doi: https://doi.org/10.1016/S1474-4422(04)00740-9. URL https://www.sciencedirect.com/science/article/pii/S1474442204007409.

[50] Elmar H. Pinkhardt and Jan Kassubek. Ocular motor abnormalities in Parkinsonian syndromes. *Parkinsonism and Related Disorders*, 17(4):223–

230, 2011. ISSN 13538020. doi: 10.1016/j.parkreldis.2010.08.004. URL http://dx.doi.org/10.1016/j.parkreldis.2010.08.004.

[51] Elmar H Pinkhardt, Reinhart Jürgens, Dorothée Lulé, Johanna Heimrath, Albert C Ludolph, Wolfgang Becker, and Jan Kassubek. Eye movement impairments in Parkinson ' s disease : possible role of extradopaminergic mechanisms. 2012.

[52] Ileok Jung and Ji-Soo Kim. Abnormal Eye Movements in Parkinsonism and Movement Disorders. *JMD*, 12(1):1–13, 1 2019. ISSN 2005-940X. doi: 10.14802/jmd.18034. URL https://doi.org/10.14802/jmd.18034 http://www.e-jmd.org/journal/view.php?number=233.

[53] Yasuo Terao, Hideki Fukuda, Akihiro Yugeta, Okihide Hikosaka, Yoshiko Nomura, Masaya Segawa, Ritsuko Hanajima, Shoji Tsuji, and Yoshikazu Ugawa. Initiation and inhibitory control of saccades with the progression of Parkinson's disease – Changes in three major drives converging on the superior colliculus. *Neuropsychologia*, 49(7):1794–1806, 2011. ISSN 0028-3932. doi: https://doi.org/10.1016/j.neuropsychologia.2011.03.002. URL https://www.sciencedirect.com/science/article/pii/S002839321100131X.

[54] Yasuo Terao, Hideki Fukuda, Yoshikazu Ugawa, and Okihide Hikosaka. New perspectives on the pathophysiology of Parkinson's disease as assessed by saccade performance: A clinical review. *Clinical Neurophysiology*, 124(8):1491–1506, 2013. ISSN 1388-2457. doi: https://doi.org/10.1016/j.clinph.2013.01.021. URL https://www.sciencedirect.com/science/article/pii/S1388245713000722.

[55] Jonathan M Chambers and Tony J Prescott. Response times for visually guided saccades in persons with Parkinson's disease: A meta-analytic review. *Neuropsychologia*, 48(4):887–899, 2010. ISSN 0028-3932. doi: https://doi.org/10.1016/j.neuropsychologia.2009.11.006. URL https://www.sciencedirect.com/science/article/pii/S0028393209004382.

[56] Aasef G Shaikh and Fatema F Ghasia. Chapter 5 - Saccades in Parkinson's disease: Hypometric, slow, and maladaptive. In Stefano Ramat and Aasef G B T Progress in Brain Research Shaikh, editors, *Mathematical Modelling in Motor Neuroscience: State of the Art and Translation to the Clinic. Gaze Orienting Mechanisms and Disease*, volume 249, pages

81–94. Elsevier, 2019. ISBN 0079-6123. doi: https://doi.org/10.1016/bs.pbr.2019.05.001. URL https://www.sciencedirect.com/science/article/pii/S0079612319301293.

[57] OWEN B WHITE, JEAN A SAINT-CYR, R DAVID TOMLINSON, and JAMES A SHARPE. OCULAR MOTOR DEFICITS IN PARKINSON'S DISEASE: II. CONTROL OF THE SACCADIC AND SMOOTH PURSUIT SYSTEMS. *Brain*, 106 (3):571–587, 9 1983. ISSN 0006-8950. doi: 10.1093/brain/106.3.571. URL https://doi.org/10.1093/brain/106.3.571.

[58] Jonathan W. Mink. The basal ganglia: Focused selection and inhibition of competing motor programs. *Progress in Neurobiology*, 50(4):381–425, 1996. ISSN 03010082. doi: 10.1016/S0301-0082(96)00042-1. URL https://pubmed.ncbi.nlm.nih.gov/9004351/.

[59] Claire Ewenczyk, Salma Mesmoudi, Cécile Gallea, Marie-Laure Welter, Bertrand Gaymard, Adèle Demain, Lydia Yahia Cherif, Bertrand Degos, Habib Benali, Pierre Pouget, Cyril Poupon, Stéphane Lehericy, Sophie Rivaud-Péchoux, and Marie Vidailhet. Antisaccades in Parkinson disease. *Neurology*, 88 (9):853 LP – 861, 2 2017. doi: 10.1212/WNL.0000000000003658. URL http://n.neurology.org/content/88/9/853.abstract.

[60] Cécile Gallea, Benoit Wicki, Claire Ewenczyk, Sophie Rivaud-Péchoux, Lydia Yahia-Cherif, Pierre Pouget, Marie Vidailhet, and Elodie Hainque. Antisaccade, a predictive marker for freezing of gait in Parkinson's disease and gait/gaze network connectivity. *Brain*, 144(2):504–514, 2 2021. ISSN 0006-8950. doi: 10.1093/brain/awaa407. URL https://doi.org/10.1093/brain/awaa407.

[61] Anke H. Snijders, Kaoru Takakusaki, Bettina Debu, Andres M. Lozano, Vibhor Krishna, Alfonso Fasano, Tipu Z. Aziz, Stella M. Papa, Stewart A. Factor, and Mark Hallett. Physiology of freezing of gait. *Annals of Neurology*, 80(5):644–659, 2016. ISSN 15318249. doi: 10.1002/ana.24778.

[62] Chiung-Chu Chen, Chien-Hung Yeh, Hsiao-Lung Chan, Ya-Ju Chang, Po-Hsun Tu, Chih-Hua Yeh, Chin-Song Lu, Petra Fischer, Gerd Tinkhauser, Huiling Tan, and

Peter Brown. Subthalamic nucleus oscillations correlate with vulnerability to freezing of gait in patients with Parkinson's disease. *Neurobiology of Disease*, 132: 104605, 2019. ISSN 0969-9961. doi: https://doi.org/10.1016/j.nbd.2019.104605. URL https://www.sciencedirect.com/science/article/pii/S0969996119302803.

[63] Mesbah Alam, Kerstin Schwabe, and Joachim K Krauss. The pedunculopontine nucleus area: critical evaluation of interspecies differences relevant for its use as a target for deep brain stimulation. *Brain*, 134(1):11–23, 1 2011. ISSN 0006-8950. doi: 10.1093/brain/awq322. URL https://doi.org/10.1093/brain/awq322.

[64] James M Shine, Elie Matar, Philip B Ward, Michael J Frank, Ahmed A Moustafa, Mark Pearson, Sharon L Naismith, and Simon J G Lewis. Freezing of gait in Parkinson's disease is associated with functional decoupling between the cognitive control network and the basal ganglia. *Brain*, 136(12):3671–3681, 12 2013. ISSN 0006-8950. doi: 10.1093/brain/awt272. URL https://doi.org/10.1093/brain/awt272.

[65] Simon J G Lewis and James M Shine. The Next Step: A Common Neural Mechanism for Freezing of Gait. *The Neuroscientist*, 22(1):72–82, 11 2014. ISSN 1073-8584. doi: 10.1177/1073858414559101. URL https://doi.org/10.1177/1073858414559101.

[66] María José Gallardo, Juan Pablo Cabello, María Jesus Corrales, Javier Torres-Donaire, Jose Javier Bravo, María Prado Talavera, Alberto León, and Julia Vaamonde-Gamo. Freezing of gait in Parkinson's disease: functional neuroimaging studies of the frontal lobe. *Neurological Research*, 40(10):900–905, 10 2018. ISSN 0161-6412. doi: 10.1080/01616412.2018.1484985. URL https://doi.org/10.1080/01616412.2018.1484985.

[67] Francois Windels, Wesley Thevathasan, Peter Silburn, and Pankaj Sah. Where and what is the PPN and what is its role in locomotion? *Brain*, 138(5):1133–1134, 5 2015. ISSN 0006-8950. doi: 10.1093/brain/awv059. URL https://doi.org/10.1093/brain/awv059.

[68] Brian Lau, Marie-Laure Welter, Hayat Belaid, Sara Fernandez Vidal, Eric Bardinet, David Grabli, and Carine Karachi. The integrative role of the pedunculopontine nucleus in human

gait. *Brain*, 138(5):1284–1296, 5 2015. ISSN 0006-8950. doi: 10.1093/brain/awv047. URL https://doi.org/10.1093/brain/awv047.

[69] Ken ichi Okada and Yasushi Kobayashi. Fixational saccade-related activity of pedunculopontine tegmental nucleus neurons in behaving monkeys. *European Journal of Neuroscience*, 40(4):2641–2651, 2014. ISSN 14609568. doi: 10.1111/ejn.12632.

[70] Robert H. Wurtz, Marc A. Sommer, Martin Paré, and Stefano Ferraina. Signal transformations from cerebral cortex to superior colliculus for the generation of saccades. *Vision Research*, 41(25-26):3399–3412, 2001. ISSN 00426989. doi: 10.1016/S0042-6989(01)00066-9.

[71] Peter A Pahapill and Andres M Lozano. The pedunculopontine nucleus and Parkinson's disease. *Brain*, 123(9):1767–1783, 9 2000. ISSN 0006-8950. doi: 10.1093/brain/123.9.1767. URL https://doi.org/10.1093/brain/123.9.1767.

[72] Yasushi Kobayashi, Yasuhiko Saito, and Tadashi Isa. Facilitation of saccade initiation by brainstem cholinergic system. *Brain and Development*, 23:S24–S27, 2001. ISSN 0387-7604. doi: https://doi.org/10.1016/S0387-7604(01)00330-8. URL https://www.sciencedirect.com/science/article/pii/S0387760401003308.

[73] A. Khaldi, E. Daniel, L. Massin, C. Kärnfelt, F. Ferranti, C. Lahuec, F. Seguin, V. Nourrit, and J. L. de Bougrenet de la Tocnaye. A laser emitting contact lens for eye tracking. *Scientific Reports*, 10(1):1–8, 2020. ISSN 20452322. doi: 10.1038/s41598-020-71233-1. URL https://doi.org/10.1038/s41598-020-71233-1.

[74] Giuseppe Micieli, Cristina Tassorelli, Emilia Martignoni, Claudio Pacchetti, Patrizia Bruggi, Marco Magri, and Giuseppe Nappi. Disordered pupil reactivity in Parkinson's disease. *Clinical Autonomic Research*, 1(1):55–58, 1991. ISSN 1619-1560. doi: 10.1007/BF01826058. URL https://doi.org/10.1007/BF01826058.

[75] S G Manohar and M Husain. Reduced pupillary reward sensitivity in Parkinson's disease. *npj Parkinson's Disease*, 1:15026, 12 2015. doi: 10.1038/npjparkd.2015.26. URL http://dx.doi.org/10.1038/npjparkd.2015.26.

[76] Chin An Wang, Hailey McInnis, Donald C. Brien, Giovanna Pari, and Douglas P. Munoz. Disruption of pupil size modulation correlates with voluntary motor preparation deficits in Parkinson's disease. *Neuropsychologia*, 80:176–184, 2016. ISSN 18733514. doi: 10.1016/j.neuropsychologia.2015.11.019. URL http://dx.doi.org/10.1016/j.neuropsychologia.2015.11.019.

[77] René J Huster, Stefanie Enriquez-Geppert, Christina F Lavallee, Michael Falkenstein, and Christoph S Herrmann. Electroencephalography of response inhibition tasks: functional networks and cognitive contributions. *International Journal of Psychophysiology*, 87(3):217–233, 3 2013. doi: 10.1016/j.ijpsycho.2012.08.001. URL http://dx.doi.org/10.1016/j.ijpsycho.2012.08.001.

[78] M Mattia, S Spadacenta, L Pavone, P Quarato, V Esposito, A Sparano, F Sebastiano, G Di Gennaro, R Morace, G Cantore, and G Mirabella. Stop-event-related potentials from intracranial electrodes reveal a key role of premotor and motor cortices in stopping ongoing movements. *Frontiers in Neuroengineering*, 5:12, 6 2012. doi: 10.3389/fneng.2012.00012. URL http://dx.doi.org/10.3389/fneng.2012.00012.

[79] Liisa Raud, René Westerhausen, Niamh Dooley, and René J Huster. Differences in unity: the go/no-go and stop signal tasks rely on different inhibitory mechanisms. *BioRxiv*, 7 2019. doi: 10.1101/705079. URL http://biorxiv.org/lookup/doi/10.1101/705079.

[80] Jan R Wessel, Darcy A Waller, and Jeremy Dw Greenlee. Non-selective inhibition of inappropriate motor-tendencies during response-conflict by a fronto-subthalamic mechanism. *eLife*, 8, 5 2019. ISSN 2050-084X. doi: 10.7554/eLife.42959.

[81] Jan R Wessel, Ayda Ghahremani, Kaviraja Udupa, Utpal Saha, Suneil K Kalia, Mojgan Hodaie, Andres M Lozano, Adam R Aron, and Robert Chen. Stop-related subthalamic beta activity indexes global motor suppression in Parkinson's disease. *Movement Disorders*, 31(12):1846–1853, 7 2016. doi: 10.1002/mds.26732. URL http://dx.doi.org/10.1002/mds.26732.

[82] Jeggan Tiego, Renee Testa, Mark A Bellgrove, Christos Pantelis, and

Sarah Whittle. A Hierarchical Model of Inhibitory Control , 2018. URL https://www.frontiersin.org/article/10.3389/fpsyg.2018.01339.

[83] Shahab Bakhtiari, Ayca Altinkaya, Christopher C. Pack, and Abbas F. Sadikot. The Role of the Subthalamic Nucleus in Inhibitory Control of Oculomotor Behavior in Parkinson's Disease. *Scientific Reports*, 10(1):1–11, 2020. ISSN 20452322. doi: 10.1038/s41598-020-61572-4.

[84] Cheol Soh and Jan R Wessel. Unexpected sounds non-selectively inhibit active visual stimulus representations. *BioRxiv*, 4 2020. doi: 10.1101/2020.04.16.044966. URL http://biorxiv.org/lookup/doi/10.1101/2020.04.16.044966.

[85] Jan R Wessel. A Neural Mechanism for Surprise-related Interruptions of Visuospatial Working Memory. *Cerebral Cortex*, 28(1):199–212, 1 2018. ISSN 1047-3211. doi: 10.1093/cercor/bhw367. URL https://doi.org/10.1093/cercor/bhw367.

[86] Fabrice B R Parmentier, Gregory Elford, Carles Escera, Pilar Andrés, and Iria San Miguel. The cognitive locus of distraction by acoustic novelty in the cross-modal oddball task. *Cognition*, 106(1):408–432, 2008. ISSN 0010-0277. doi: https://doi.org/10.1016/j.cognition.2007.03.008. URL https://www.sciencedirect.com/science/article/pii/S0010027707000832.

[87] Michael E Dawson, Anne M Schell, James R Beers, and Andrew Kelly. Allocation of cognitive processing capacity during human autonomic classical conditioning. *Journal of Experimental Psychology: General*, 111(3):273–295, 1982. ISSN 1939-2222. doi: 10.1037/0096-3445.111.3.273.

[88] Jan R Wessel and Adam R Aron. On the Globality of Motor Suppression: Unexpected Events and Their Influence on Behavior and Cognition. *Neuron*, 93(2):259–280, 2017. ISSN 0896-6273. doi: https://doi.org/10.1016/j.neuron.2016.12.013. URL https://www.sciencedirect.com/science/article/pii/S0896627316309552.

[89] Andreas Meinel, Juan Sebastian Castaño-Candamil, Sven Dähne, Janine Reis, and Michael Tangermann. EEG band power predicts single-trial reaction time in a hand motor task.

International IEEE/EMBS Conference on Neural Engineering, NER, 2015-July:182–185, 2015. ISSN 19483554. doi: 10.1109/NER.2015.7146590.

[90] William Beam, Jeffrey J Borckardt, Scott T Reeves, and Mark S George. An efficient and accurate new method for locating the F3 position for prefrontal {TMS} applications. *Brain Stimulation*, 2(1):50–54, 1 2009. doi: 10.1016/j.brs.2008.09.006. URL http://dx.doi.org/10.1016/j.brs.2008.09.006.

[91] Tristan Stenner and Chadwick Boulay. Lab Streaming Layer GitHub, 2021. URL https://labstreaminglayer.readthedocs.io/index.html.

[92] Nikolai Smetanin, Ksenia Volkova, Stanislav Zabodaev, Mikhail A Lebedev, and Alexei Ossadtchi. NFBLab-A Versatile Software for Neurofeedback and Brain-Computer Interface Research. *Frontiers in Neuroinformatics*, 12:100, 12 2018. doi: 10.3389/fninf.2018.00100. URL http://dx.doi.org/10.3389/fninf.2018.00100.

[93] Fiorenzo Artoni, Annalisa Barsotti, Eleonora Guanziroli, Silvestro Micera, Alberto Landi, and Franco Molteni. Effective synchronization of {EEG} and {EMG} for mobile brain/-body imaging in clinical settings. *Frontiers in Human Neuroscience*, 11:652, 2017. doi: 10.3389/fnhum.2017.00652. URL http://dx.doi.org/10.3389/fnhum.2017.00652.

[94] Robert Riener and Matthias Harders. *Virtual Reality in Medicine*, volume 9781447140. Springer London, London, 2012. ISBN 978-1-4471-4010-8. doi: 10.1007/978-1-4471-4011-5. URL http://link.springer.com/10.1007/978-1-4471-4011-5.

[95] G Székely and R M Satava. Virtual reality in medicine. Interview by Judy Jones. *BMJ (Clinical research ed.)*, 319(7220):1305, 11 1999. ISSN 0959-8138. doi: 10.1136/bmj.319.7220.1305. URL https://pubmed.ncbi.nlm.nih.gov/10559057 https://www.ncbi.nlm.nih.gov/pmc/articles/PMC1129082/.

[96] Ruby Sharma. Visual Evoked Potentials: Normative Values and Gender Differences. *JOURNAL OF CLINICAL AND DIAGNOSTIC RESEARCH*, 9(7):{CC12}–5, 7 2015. ISSN 2249782X. doi: 10.7860/JCDR/2015/12764.6181.

[97] James J Stockard, Jane F Hughes, and Frank W Sharbrough. Visually Evoked Potentials to Electronic Pattern Reversal: Latency Variations with Gender, Age, and Technical Factors. *American Journal of EEG Technology*, 19(4): 171–204, 12 1979. ISSN 0002-9238. doi: 10.1080/00029238.1979.11079986. URL https://www.tandfonline.com/doi/full/10.1080/00029238.1979.11079986.

[98] P Walsh, N Kane, and S Butler. The clinical role of evoked potentials. *Journal of Neurology, Neurosurgery, and Psychiatry*, 76 Suppl 2:16–22, 6 2005. doi: 10.1136/jnnp.2005.068130. URL http://dx.doi.org/10.1136/jnnp.2005.068130.

[99] Gernot G Supp, Focko L Higgen, Joerg F Hipp, Andreas K Engel, and Markus Siegel. Mid-Latency Auditory Evoked Potentials Differentially Predict Sedation and Drug Level Under Opioid and Hypnotic Agents. *Frontiers in pharmacology*, 9:1427, 12 2018. doi: 10.3389/fphar.2018.01427. URL http://dx.doi.org/10.3389/fphar.2018.01427.

[100] Guy Lightfoot. Summary of the N1-P2 Cortical Auditory Evoked Potential to Estimate the Auditory Threshold in Adults. *Seminars in hearing*, 37(1):1–8, 2 2016. doi: 10.1055/s-0035-1570334. URL http://dx.doi.org/10.1055/s-0035-1570334.

[101] Kip A Ludwig, Rachel M Miriani, Nicholas B Langhals, Michael D Joseph, David J Anderson, and Daryl R Kipke. Using a common average reference to improve cortical neuron recordings from microelectrode arrays. *Journal of Neurophysiology*, 101(3):1679–1689, 3 2009. doi: 10.1152/jn.90989.2008. URL http://dx.doi.org/10.1152/jn.90989.2008.

[102] Andreas Widmann, Erich Schröger, and Burkhard Maess. Digital filter design for electrophysiological data–a practical approach. *Journal of Neuroscience Methods*, 250:34–46, 7 2015. doi: 10.1016/j.jneumeth.2014.08.002. URL http://dx.doi.org/10.1016/j.jneumeth.2014.08.002.

[103] Rajesh P.N. Rao and Reinhold Scherer. Statistical Pattern Recognition and Machine Learning in Brain-Computer Interfaces. In *Statistical Signal Processing for Neuroscience and Neurotechnology*, pages 335–367. Elsevier Inc., 1 2010. ISBN 9780123750273. doi: 10.1016/B978-0-12-375027-3.00010-7.

[104] Shravani Sur and V K Sinha. Event-related potential: An overview. *Industrial psychiatry journal*, 18(1):70–73, 1 2009. doi: 10.4103/0972-6748.57865. URL http://dx.doi.org/10.4103/0972-6748.57865.

[105] T. Radüntz, J. Scouten, O. Hochmuth, and B. Meffert. EEG artifact elimination by extraction of ICA-component features using image processing algorithms. *Journal of Neuroscience Methods*, 243:84–93, 3 2015. ISSN 1872678X. doi: 10.1016/j.jneumeth.2015.01.030.

[106] Richard J Samworth and Ming Yuan. Independent component analysis via nonparametric maximum likelihood estimation. *The Annals of Statistics*, 40(6): 2973–3002, 12 2012. ISSN 0090-5364. doi: 10.1214/12-{AOS1060}. URL http://projecteuclid.org/euclid.aos/1360332190.

[107] David J C MacKay. Maximum Likelihood and Covariant Algorithms for Independent Component Analysis. 1996. URL http://citeseerx.ist.psu.edu/viewdoc/summary?doi=10.1.1.48.120.

[108] Eric Moreau and Tülay Adali. Maximum Likelihood {ICA}. In *Blind Identification and Separation of Complex-Valued Signals*, pages 47–81. John Wiley & Sons, Inc., Hoboken, {NJ} {USA}, 9 2013. ISBN 9781118579749. doi: 10.1002/9781118579749.ch3. URL http://doi.wiley.com/10.1002/9781118579749.ch3.

[109] Alexandre Gramfort, Martin Luessi, Eric Larson, Denis Engemann, Daniel Strohmeier, Christian Brodbeck, Roman Goj, Mainak Jas, Teon Brooks, Lauri Parkkonen, and Matti Hämäläinen. MEG and EEG data analysis with MNE-Python , 2013. URL https://www.frontiersin.org/article/10.3389/fnins.2013.00267.

[110] Matar Haller, Thomas Donoghue, Erik Peterson, Paroma Varma, Priyadarshini Sebastian, Richard Gao, Torben Noto, Robert T Knight, Avgusta Shestyuk, and Bradley Voytek. Parameterizing neural power spectra. *bioRxiv*, page 299859, 1 2018. doi: 10.1101/299859. URL https://doi.org/10.1101/299859 http://biorxiv.org/content/early/2018/04/11/299859.abstract.

[111] Hung Ming Wu, Fu Jung Hsiao, Rou Shayn Chen, Din E. Shan, Wan Yu Hsu, Ming Chang

Chiang, and Yung Yang Lin. Attenuated NoGo-related beta desynchronisation and synchronisation in Parkinson's disease revealed by magnetoencephalographic recording. *Scientific Reports*, 9(1):1–12, 12 2019. ISSN 20452322. doi: 10.1038/s41598-019-43762-x. URL https://doi.org/10.1038/s41598-019-43762-x.

[112] Bernadette C.M. van Wijk, Martijn Beudel, Ashwani Jha, Ashwini Oswal, Tom Foltynie, Marwan I. Hariz, Patricia Limousin, Ludvic Zrinzo, Tipu Z. Aziz, Alexander L. Green, Peter Brown, and Vladimir Litvak. Subthalamic nucleus phase-amplitude coupling correlates with motor impairment in Parkinson's disease. *Clinical Neurophysiology*, 127(4):2010–2019, 2016. ISSN 18728952. doi: 10.1016/j.clinph.2016.01.015. URL http://dx.doi.org/10.1016/j.clinph.2016.01.015.

[113] Nicole C. Swann, Coralie De Hemptinne, Adam R. Aron, Jill L. Ostrem, Robert T. Knight, and Philip A. Starr. Elevated synchrony in Parkinson disease detected with electroencephalography. *Annals of Neurology*, 78(5):742–750, 11 2015. ISSN 15318249. doi: 10.1002/ana.24507. URL /pmc/articles/PMC4623949/?report=abstract https://www.ncbi.nlm.nih.gov/pmc/articles/PMC4623949/.

[114] Roxanne Lofredi, Huiling Tan, Wolf Julian Neumann, Chien Hung Yeh, Gerd Helge Schneider, Andrea A. Kühn, and Peter Brown. Beta bursts during continuous movements accompany the velocity decrement in Parkinson's disease patients. *Neurobiology of Disease*, 127:462–471, 7 2019. ISSN 1095953X. doi: 10.1016/j.nbd.2019.03.013. URL https://doi.org/10.1016/j.nbd.2019.03.013.

[115] Gerd Tinkhauser, Flavie Torrecillos, Yann Duclos, Huiling Tan, Alek Pogosyan, Petra Fischer, Romain Carron, Marie-Laure Laure Welter, Carine Karachi, Wim Vandenberghe, Bart Nuttin, Tatiana Witjas, Jean Régis, Jean-Philippe Philippe Azulay, Alexandre Eusebio, and Peter Brown. Beta burst coupling across the motor circuit in Parkinson's disease. *Neurobiology of Disease*, 117:217–225, 6 2018. ISSN 1095953X. doi: 10.1016/j.nbd.2018.06.007. URL http://dx.doi.org/10.1016/j.nbd.2018.06.007 http://creativecommons.org/licenses/BY/4.0/.

[116] Gerd Tinkhauser, Ahmar Syed Shah, Petra Fischer, Katrin Peterman, Ines Debove,

Khoa Nygyuen, Andreas Nowacki, Flavie Torrecillos, Saed Khawaldeh, Huiling Tan, Alek Pogosyan, Michael Schuepbach, Claudio Pollo, and Peter Brown. Electrophysiological differences between upper and lower limb movements in the human subthalamic nucleus. *Clinical Neurophysiology*, 130(5):727–738, 5 2019. ISSN 18728952. doi: 10.1016/j.clinph.2019.02.011. URL `https://doi.org/10.1016/j.clinph.2019.02.011`.

[117] Matteo Demuru and Matteo Fraschini. EEG fingerprinting: Subject-specific signature based on the aperiodic component of power spectrum. *Computers in Biology and Medicine*, 120:103748, 5 2020. ISSN 18790534. doi: 10.1016/j.compbiomed.2020.103748.

[118] Eleni Chiou and Sadasivan Puthusserypady. Spatial filter feature extraction methods for P300 {BCI} speller: A comparison. In *2016 {IEEE} International Conference on Systems, Man, and Cybernetics ({SMC})*, pages 3859–3863. IEEE, 10 2016. ISBN 978-1-5090-1897-0. doi: 10.1109/SMC.2016.7844836. URL `http://ieeexplore.ieee.org/document/7844836/`.

[119] Bertrand Rivet, Antoine Souloumiac, Virginie Attina, and Guillaume Gibert. xDAWN Algorithm to Enhance Evoked Potentials: Application to Brain–Computer Interface. *IEEE Transactions on Biomedical Engineering*, 56(8):2035–2043, 8 2009. ISSN 0018-9294. doi: 10.1109/TBME.2009.2012869.

[120] Mohammad Jalilpour Monesi and Sepideh Hajipour Sardouie. Extended common spatial and temporal pattern (ECSTP): A semi-blind approach to extract features in ERP detection. *Pattern Recognition*, 95:128–135, 11 2019. ISSN 00313203. doi: 10.1016/j.patcog.2019.05.039. URL `https://www.sciencedirect.com/science/article/pii/S0031320319302249`.

[121] Daniel Álvarez, Ana Cerezo-Hernández, Andrea Crespo, Gonzalo C Gutiérrez-Tobal, Fernando Vaquerizo-Villar, Verónica Barroso-García, Fernando Moreno, C Ainhoa Arroyo, Tomás Ruiz, Roberto Hornero, and Félix del Campo. A machine learning-based test for adult sleep apnoea screening at home using oximetry and airflow. *Scientific Reports*, 10(1):5332, 2020. ISSN 2045-2322. doi: 10.1038/s41598-020-62223-4. URL `https://doi.org/10.1038/s41598-020-62223-4`.

[122] Sid Ahmed Belhadj, Nawal Benmoussat, and Mohamed Della Krachai. CSP features extraction and FLDA classification of EEG-based motor imagery for Brain-Computer Interaction. In *2015 4th International Conference on Electrical Engineering (ICEE)*, pages 1–6. IEEE, 12 2015. ISBN 978-1-4673-6673-1. doi: 10.1109/INTEE.2015.7416697.

[123] Kai Keng Ang, Zhang Yang Chin, Haihong Zhang, and Cuntai Guan. Filter Bank Common Spatial Pattern (FBCSP) in Brain-Computer Interface. In *2008 IEEE International Joint Conference on Neural Networks (IEEE World Congress on Computational Intelligence)*, pages 2390–2397. IEEE, 6 2008. ISBN 978-1-4244-1820-6. doi: 10.1109/IJCNN.2008.4634130. URL http://ieeexplore.ieee.org/document/4634130/.

[124] Peiyang Li, Peng Xu, Rui Zhang, Lanjin Guo, and Dezhong Yao. L1 Norm based common spatial patterns decomposition for scalp EEG BCI. *BioMedical Engineering OnLine*, 12 (1):77, 8 2013. ISSN 1475-925X. doi: 10.1186/1475-925X-12-77.

[125] Christoph Bergmeir and José M Benítez. On the use of cross-validation for time series predictor evaluation. *Information Sciences*, 191:192–213, 2012. ISSN 0020-0255. doi: https://doi.org/10.1016/j.ins.2011.12.028. URL https://www.sciencedirect.com/science/article/pii/S0020025511006773.

[126] Andrew W Moore and Mary S Lee. Efficient Algorithms for Minimizing Cross Validation Error. In William W Cohen and Haym B T Machine Learning Proceedings 1994 Hirsh, editors, *Machine Learning Proceedings 1994*, pages 190–198. Morgan Kaufmann, San Francisco (CA), 1994. ISBN 978-1-55860-335-6. doi: https://doi.org/10.1016/B978-1-55860-335-6.50031-3. URL https://www.sciencedirect.com/science/article/pii/B9781558603356500313.

[127] Fabian Pedregosa, Gaël Varoquaux, Alexandre Gramfort, Vincent Michel, Bertrand Thirion, Olivier Grisel, Mathieu Blondel, Peter Prettenhofer, Ron Weiss, Vincent Dubourg, Jake Vanderplas, Alexandre Passos, David Cournapeau, Matthieu Brucher, Matthieu Perrot, and Edouard Duchesnay. Scikit-learn: Machine Learning in Python. *Journal of Machine Learning Research*, 12(85):2825–2830, 2011. URL http://jmlr.org/papers/v12/pedregosa11a.html.

[128] Esteban Real, Chen Liang, David R. So, and Quoc V. Le. AutoML-Zero: Evolving Machine Learning Algorithms From Scratch. *arXiv*, 3 2020. URL http://arxiv.org/abs/2003.03384.

[129] D Mukunthu, P Shah, and W H Tok. *Practical Automated Machine Learning on Azure: Using Azure Machine Learning to Quickly Build AI Solutions*. O'Reilly Media, 2019. ISBN 9781492055563. URL https://books.google.ca/books?id=tlKxDwAAQBAJ.

[130] Shan Suthaharan. Support Vector Machine BT - Machine Learning Models and Algorithms for Big Data Classification: Thinking with Examples for Effective Learning. pages 207–235. Springer US, Boston, MA, 2016. ISBN 978-1-4899-7641-3. doi: 10.1007/978-1-4899-7641-3$_$9.

[131] William S Noble. What is a support vector machine? *Nature Biotechnology*, 24(12): 1565–1567, 2006. ISSN 1546-1696. doi: 10.1038/nbt1206-1565.

[132] Derek A Pisner and David M Schnyer. Chapter 6 - Support vector machine. pages 101–121. Academic Press, 2020. ISBN 978-0-12-815739-8. doi: https://doi.org/10.1016/B978-0-12-815739-8.00006-7. URL https://www.sciencedirect.com/science/article/pii/B9780128157398000067.

[133] Xingye Qiao and Lingsong Zhang. Distance-weighted Support Vector Machine. 10 2013. URL http://arxiv.org/abs/1310.3003.

[134] Thais Mayumi Oshiro, Pedro Santoro Perez, and José Augusto Baranauskas. How Many Trees in a Random Forest? BT - Machine Learning and Data Mining in Pattern Recognition. pages 154–168, Berlin, Heidelberg, 2012. Springer Berlin Heidelberg. ISBN 978-3-642-31537-4. doi: https://doi.org/10.1007/978-3-642-31537-4_13.

[135] M Pal. Random forest classifier for remote sensing classification. *International Journal of Remote Sensing*, 26(1):217–222, 1 2005. ISSN 0143-1161. doi: 10.1080/01431160412331269698.

[136] Leo Breiman. Random Forests. *Machine Learning*, 45(1):5–32, 2001. ISSN 1573-0565. doi: 10.1023/A:1010933404324. URL https://doi.org/10.1023/A:1010933404324.

[137] Harsh Chawla and Hemant Kathuria. Azure Kubernetes Service BT - Building Microservices Applications on Microsoft Azure: Designing, Developing, Deploying, and Monitoring. pages 151–177. Apress, Berkeley, CA, 2019. ISBN 978-1-4842-4828-7. doi: 10.1007/978-1-4842-4828-7$_$5.

[138] Suresh D. Muthukumaraswamy. High-frequency brain activity and muscle artifacts in MEG/EEG: a review and recommendations. *Frontiers in Human Neuroscience*, 7:138, 2013. ISSN 1662-5161. doi: 10.3389/fnhum.2013.00138.

[139] Ian Greenhouse and Jan R Wessel. EEG signatures associated with stopping are sensitive to preparation. *Psychophysiology*, 50(9):900–908, 9 2013. doi: 10.1111/psyp.12070. URL `http://dx.doi.org/10.1111/psyp.12070`.

[140] Irene Winkler, Stefan Haufe, and Michael Tangermann. Automatic Classification of Artifactual ICA-Components for Artifact Removal in EEG Signals. *Behavioral and Brain Functions*, 7(1):30, 2011. ISSN 1744-9081. doi: 10.1186/1744-9081-7-30. URL `https://doi.org/10.1186/1744-9081-7-30`.

[141] Megan Hynd, Cheol Soh, Benjamin O Rangel, and Jan R Wessel. Paired-pulse TMS and scalp EEG reveal systematic relationship between inhibitory GABAa signaling in M1 and fronto-central cortical activity during action stopping. *Journal of Neurophysiology*, 125(2):648–660, 1 2021. ISSN 0022-3077. doi: 10.1152/jn.00571.2020. URL `https://doi.org/10.1152/jn.00571.2020`.

[142] Andrew P Bradley. The use of the area under the ROC curve in the evaluation of machine learning algorithms. *Pattern Recognition*, 30(7):1145–1159, 7 1997. ISSN 00313203. doi: 10.1016/S0031-3203(96)00142-2.

[143] Gavin C Cawley and Nicola L C Talbot. On over-fitting in model selection and subsequent selection bias in performance evaluation. *The Journal of Machine Learning Research*, 11: 2079–2107, 2010. ISSN 1532-4435.

[144] Moritz Kassner, William Patera, and Andreas Bulling. Pupil: An Open Source Platform for Pervasive Eye Tracking and Mobile Gaze-Based Interaction. In *Proceedings of the 2014*

ACM International Joint Conference on Pervasive and Ubiquitous Computing: Adjunct Publication, UbiComp '14 Adjunct, page 1151–1160, New York, NY, USA, 2014. Association for Computing Machinery. ISBN 9781450330473. doi: 10.1145/2638728.2641695. URL https://doi.org/10.1145/2638728.2641695.

[145] Intheon. Neuropype. URL https://www.neuropype.io.

[146] Thomas Donoghue, Matar Haller, Erik J Peterson, Paroma Varma, Priyadarshini Sebastian, Richard Gao, Torben Noto, Antonio H Lara, Joni D Wallis, Robert T Knight, Avgusta Shestyuk, and Bradley Voytek. Parameterizing neural power spectra into periodic and aperiodic components. *Nature Neuroscience*, 23(12):1655–1665, 2020. ISSN 1546-1726. doi: 10.1038/s41593-020-00744-x. URL https://doi.org/10.1038/s41593-020-00744-x.

8 Appendix

8.1 Experimental Platform

The experimental platform was constructed to support the latest LTS release of Unity3D, which is version 2020.3.0 as of writing. The experimental platform is actively maintained and binaries will be available upon request. Detailed instructions including platform specific procedures are outlined in the repository README.

8.1.1 Eye-Tracking Calibration

The Pupil Labs eye-tracker plugin for Unity was adopted for the experimental platform, and the calibration routines were built-in with the experimenter GUI [144]. Upon start, the experimenter ensured the eye-tracker could construct a model of the participant's eyes with high confidence, indicated in the Pupil Labs capture software (Figure 17). The calibration process was initiated with the GUI controls resulting in a sequence of displayed points where the subject fixated. After calibration, the experimenter viewed the estimated gaze locations overlying fixation points using the GUI to determine whether re-calibration was necessary.

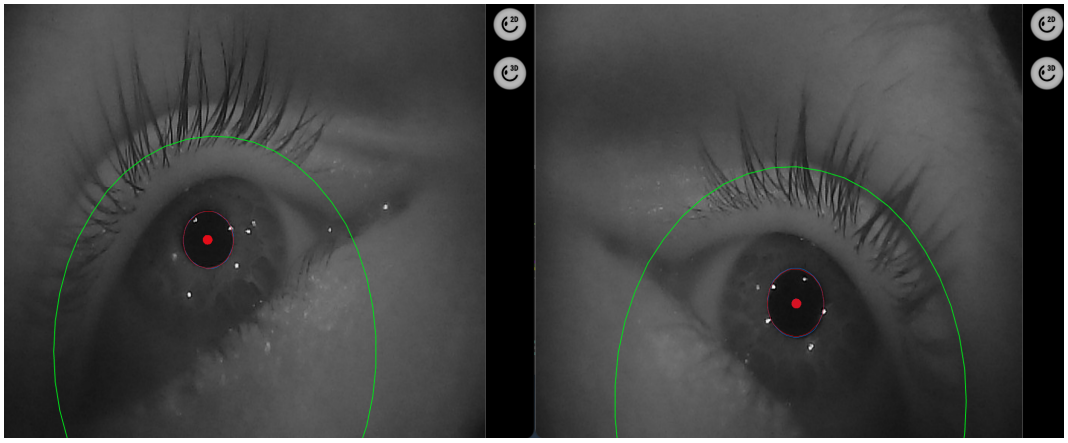

Figure 17: Successful tuning of the eye cameras would display a red circle around the pupil and a green circle for the eye model.

8.1.2 LabRecorder and Data Streams

The LSL GitHub repository provided software for streaming continuous data over the network from the connected hardware. Each connected device was present in the software LabRecorder, which was used to detect the available streams for recording (Figure 18). Once all the devices were subscribed, the recording could begin.

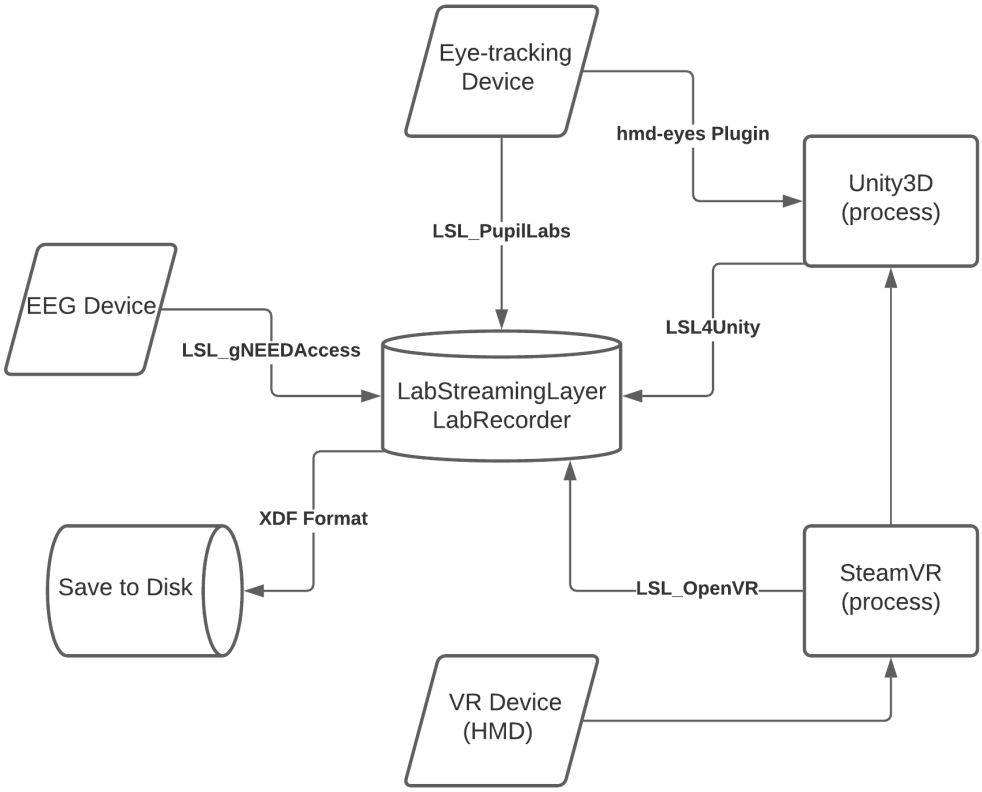

Figure 18: Sample EEG experiment setup with LSL used to aggregate devices on LSL's unified clock.

The analysis of neural recordings relies on accurately reconstructing the recorded trials to allow feature extraction appropriately aligned with behavioural events on a trial-by-trial basis. Although strong evoked potentials in response to sensory stimuli could be reliably examined even in the presence of jitter, precise features such as phase synchrony are difficult to investigate if timestamps are inconsistent. Therefore, to ensure that stimulus events occured when they were

LabStreamingLayer Data Streams		
Data Stream	Stream Type	Sampling Rate
Event Markers	Markers	Irregular
PupilLabs EyeTracker	Data	120 Hz
Blackrock Microsystems	Data	30000 Hz
HMD	Data	1000 Hz

Table 3: Intraoperative memory-guided saccade task recording setup. Data streams transmitted through lab streaming layer have different sampling rates and can be synchronized for data analysis.

LabStreamingLayer Data Streams		
Data Stream	Stream Type	Sampling Rate
Event Markers	Markers	Irregular
Tobii EyeTracker	Data	30 Hz
EEG	Data	500 Hz
HMD	Data	1000 Hz

Table 4: EEG stop signal task recording setup. Data streams transmitted through lab streaming layer have different sampling rates and can be synchronized for data analysis.

programmed to, the visual processing and trial progression delay and jitter were quantified.

8.1.3 Benchmarked Event Marker Systems

Blackrock systems contain calibrated hardware. The Blackrock comment event is inserted in the same file group as the recorded data streams, allowing the playback software to reconstruct the exact timestamp in which the comment was inserted. Serial transmission requires a specific configuration (baud rate) and is known for lower latency and jitter despite slower speeds for larger files. This system enforces a robust connection during experiments as the configurations of both the sender and receiver are explicitly defined, which eliminates the overhead and other processes during the transmission of information. We tested the LSL markers against this system, and LSL markers are events sent over the network stream.

8.1.4 Unity3D: Virtual Reality

Unity3D is game engine that provides designers tools for developing 3-dimensional environments, and delivers real-time interactive images that can be displayed on multiple platforms. Unity3D's constant updates, active community, and wide range of support for VR devices makes the engine a favourable tool for neurophysiology researchers. We used Unity3D to create the

3D environments used in our experiments. The lab streaming layer plugin for Unity3D enables the different data acquisition sources to interface with each other. This includes transferring the eye-tracker calibration and real-time gaze data to the 3D environment. Our current design has fixed objects in the experimental tasks, however the lab streaming layer allows it to extend to the capability of manipulating 3D objects in real-time with neural data, which we anticipate in future brain-computer interface experiments.

8.1.5 Visual Processing Latency and Jitter of the VR Equipment

To measure the visual processing latency and jitter of the VR head-mounted display (HMD), a photoresistor was connected to the Blackrock Cerebus data acquisition system via a BNC cable as an analog data stream. As a separate stream, the information gathered from the photoresistor is independent and does not interfere with neural signal processing. The photoresistor was placed inside the HMD to record continuously as the Unity3D test environment displays periodic flashes. Prior to the frame of the flash, the program simultaneously sends a prompt to all three data streams: serial, comment, and LSL. The LSL clock was synchronized with the Blackrock system, and the three data streams were benchmarked relative to the photoresistor's detection of the flash. The Cerebus accurately time-stamped the initial instruction to change the VR HMD screen and when visual information was displayed on the VR HMD screen. The timestamp for the photoresistor's signal detection was acquired using Python code. The hardware latency of the photoresistor was assumed to be negligible, allowing any potential jitter of the VR equipment caused by the overhead in software and the operating system contained within the experimental platform to be determined.

```
public enum FlashState
{
    Flash, ToFlash, NoFlash, NFlashStates
}
void Update ()
{
    if (thisState == FlashState.NoFlash)
    {
        FlashNowBlack();
```

```
        thisState = FlashState.NFlashStates;
    }

    if (thisState == FlashState.Flash)
    {
        FlashNowWhite();
        thisState = FlashState.NoFlash;
    }

    if (thisState == FlashState.ToFlash)
    {
        thisState = FlashState.Flash;
    }
}
void FlashNowWhite()
{
    mainCamera.backgroundColor = Color.white;
    outCont.PublishFlash("{\"Flash\": ToWhite}");
}
void FlashNowBlack()
{
    mainCamera.backgroundColor = Color.black;
    outCont.PublishFlash("{\"Flash\": ToBlack}");
}
```

Listing 4: Code excerpt from the script handling the flash mechanism at regular intervals during the visual processing latency testing.

8.1.6 Trial progression state machine for experimental design and jitter evaluation

The Unity3D engine provides a built-in state machine commonly used by animation professionals for designing hyper-realistic movement. The states are capable of executing a set of commands until certain conditions are met, such as the movement dynamics in transitioning from standing, walking, to running; improper transitions such as standing to running are blocked.

Our platform uses the built-in state machine for trial progression by providing a flexible and generic naming schematic (Figure 19). The gate phase prohibits trial advancement until

the subject maintains fixation to the fixation point for a number of seconds. In addition, the time duration between each state can easily be changed in the development interface. The user-friendly graphical user interface enables scientists to create custom state machines for their needs, and reduces the need to constantly update the code as the API is maintained concurrently with Unity3D.

The state machine latency was benchmarked by taking the timestamps between two states that were programmed to have a constant delay between them. The standard deviation and percentage error were calculated by using the expected value as the constant delay value to compare the calculated values. A histogram was constructed and the range of the distribution would indicate the jitter characteristics.

8.1.7 PupilLabs eye tracking

The HTC Vive VR headset was modified to house the Pupil Labs binocular VR eye-tracking system. The eye cameras were positioned below and slightly lateral with respect to each eye. The eye-tracker had a tracking frequency of 120 Hz, and gaze accuracy and precision of -1.0deg and -0.08deg respectively. The camera latency is 5.7 ms with less than 4 ms of processing latency. The captured image resolution was 320x240 px and the recordings were capped at 120 frames per second.

Pupil detection is handled by algorithms designed by the open source Pupil Labs project. Prior to data collection, camera parameters were fine-tuned until pupil detection confidence was high. Pupil and gaze positions were streamed over LSL for Unity3D to process subject performance. Eye videos were recorded during the duration of the experiment.

8.2 Neurophysiology Methods

The equipment outlined in Figure 18 was approved for use in clinical research. The experimental platform was investigated for use in human volunteers. The data collected arose from behavioural tasks designed to engage and research specific neural pathways.

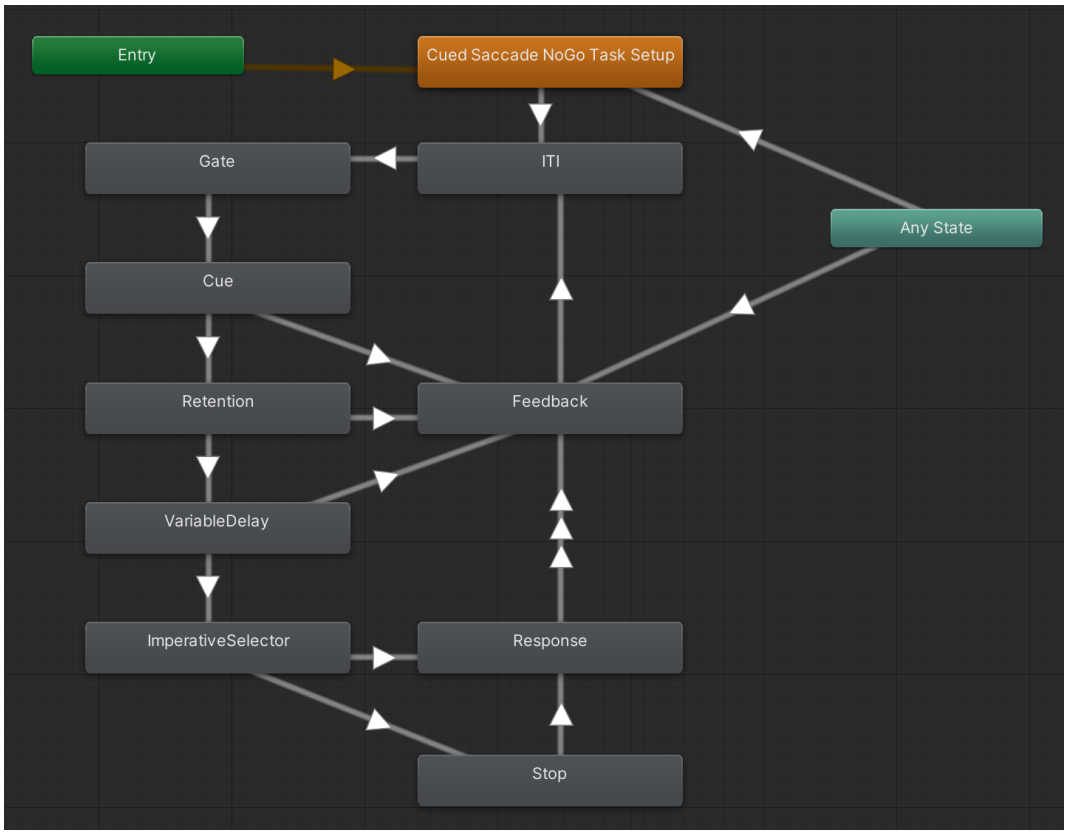

Figure 19: Unity3D State Machine repurposed for use in psychophysics experiments on a trial-by-trial basis. Sample stop-signal task to demonstrate trial progression paths: if the subject loses fixation prior to the imperative phase, the state machine will play the feedback state. If the experimenter decides to pause the experiment, the recess interface can be designed around 'Any State'.

8.2.1 Python Neuroimaging Packages

We leveraged various developmental libraries to transform the highly dimensional neural data into formats to allow further data analytics using pre-existing software, such as Neuropype and MNE. Intheon's Neuropype is a suite of tools that are frequently used in neuroimaging, neural signal processing and real-time brain-computer interfacing[145]. Our platform leverages the hierarchical data structure in Neuropype to systematically run pipelines (preprocessing, applying filters and transformations) across all subjects. MNE is an open-source Python package containing tailored workflows for neural signal processing, such as source estimation and machine learning in timeseries datasets[109].

8.2.2 Time-locked Event Related Potentials

The continuous data and the event markers operated on the same clock to align the data streams. All samples recorded in the epoch window were averaged for visualizing the ERP. Using the python developing environment in Neuropype, the epochs were constructed using the time point for the imperative phase time locked at 0.0 seconds for each trial. This imperative phase is represented by the fixation point disappearing, which prompts the user to initiate a saccade. Since each trial's imperative phase would be grouped, this phase was zeroed and labeled as 0.0 seconds in the timeseries.

8.2.3 Fitting Oscillations One Over F Analysis

Neuropype preprocessed the recorded data modalities (eye position, events, neural data, etc.) into timelocked spectrograms for FOOOF modelling. The spectrogram was computed for each trial and then passed into the FOOOF algorithm. The FOOOF algorithm provides an aperiodic component and the peaks extrapolated from the periodic component. Each computed peak has the properties of bandwidth, power, and peak frequency[146].

8.2.4 Toolboxes for data conversion

For EEG data, the session recordings were converted using Neuropype from an XDF file to a SET file for loading into the MNE toolbox. The SET file extension allows other users to use

different toolboxes, such as MNE, EEGLAB and FieldTrip. For the MER data, the python package Neo was used to preprocess the BlackRock data type, and then subsequently used in conjunction with the XDF file to align the neurophysiology data with the event data. Example scripts for demonstrating this are provided in the supplementary section.